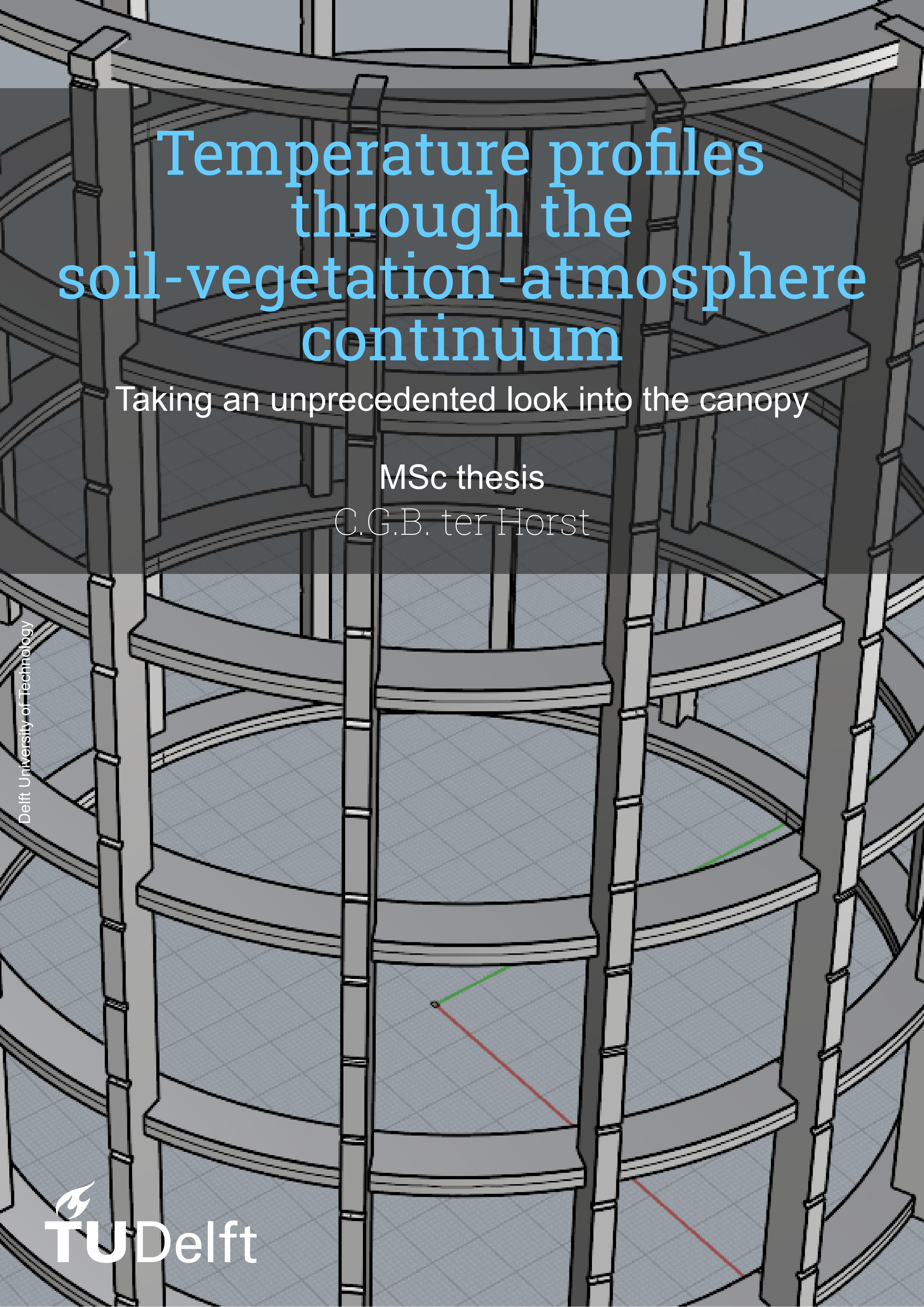

Temperature profiles through the soil-vegetation-atmosphere continuum

Taking an unprecedented look into the canopy

MSc thesis

C.G.B. ter Horst

Delft University of Technology

TUDelft

Temperature profiles through the soil-vegetation-atmosphere continuum

Taking an unprecedented look into the canopy

by

C.G.B. ter Horst

Student Name	Student Number
ter Horst	5136350

Primary Instructor and examiner:	B.J.H. van de Wiel
PhD supervisor:	G.A. Vis
Secondary instructor:	R.W. Hut
Secondary examiner:	W.G. Bouwman
Project Duration:	09, 2023 - 06, 2024
Faculty:	Faculty of applied sciences (applied physics), Delft

Cover: Tijn ter Horst, render of DTS frame design

TU Delft

Abstract

Predicting near-surface temperature profiles is an essential, yet often challenging aspect of modeling boundary layer meteorology. The surface temperature is commonly inferred from similarity relationships. These predict the vertical profiles of both wind and temperature at some height above a surface with roughness elements, such as grass. These profiles have a logarithmic shape along the vertical. Due to experimental limitations, there are very few observations in the region close to the surface where roughness elements are present. As a consequence, the logarithmic profiles are commonly extrapolated down to the surface. However, this approach is physically inconsistent at its core. Temperature gradients become infinite as the surface is approached, as a result of the logarithmic properties of the similarity profiles. One consequence is that these profiles are extremely sensitive to small perturbations close to the surface, which is a major source of uncertainty when extrapolating temperatures. To combat this, new physical models are being investigated in an attempt to describe these profiles in a more accurate and physically rigorous manner.

A broader goal in the field of atmospheric science is to study a way to unify internal canopy dynamics with the dynamics above the canopy to yield temperature profiles that are valid from the surface, through the canopy, up into the atmosphere.

In working towards these goals, a key element still lacks; precise, high resolution temperature measurements through the canopy-atmosphere interface. Novel measurement techniques such as distributed temperature sensing (DTS) have advanced the quality of datasets significantly, yielding temperature profiles with a resolution and accuracy on the order of centimeters. However, it has thus far not yielded sufficient accuracy for conclusive model comparison and for studying internal canopy temperature profiles. Therefore, there is a need for a more accurate, high-resolution dataset.

To this end, an experiment was designed to gain detailed insight into these regimes. A helical frame structure was designed, built and combined with the method of distributed temperature sensing (DTS) to attain a high resolution temperature profile along the vertical. The setup was installed at Cabauw where several weeks of data were acquired. Preliminary data analysis shows that the resulting data is well suited for the aforementioned purposes. Strong gradients near the surface can be identified as a result of the high measurement resolution on the millimeter scale. Furthermore, close to 80 data points are located within the 10cm canopy, allowing for the investigation of internal canopy transport dynamics. Finally, the data may be used in the future to validate any future models that aim to combine the canopy and atmospheric regimes.

Contents

Nomenclature

Abbreviations

Abbreviation	Definition
MOST	Monin Obukhov similarity theory
TKE	turbulent kinetic energy
ABL	atmospheric boundary layer
ASL	atmospheric surface layer
RSL	roughness sublayer
DTS	distributed temperature sensing

1 Introduction

Weather and climate models require an accurate description of near-surface temperature profiles, as these profiles determine the exchange of energy between the earth and its atmosphere. Knowledge about physical quantities such as the surface temperature is crucial for accurate atmospheric modeling [1] [2]. In this thesis we consider atmospheric flows over rough, grass-covered surfaces. Vegetation layers such as grass act as strong insulation layers between the soil and lower atmosphere, analogous to a sweater, as a layer of still air is formed within it. This property results in large temperature gradients in both the atmosphere and the soil, near the grass canopy. The global abundance of grass covered land motivates us to seek better understanding of the aforementioned properties, as it plays a significant role in atmospheric modeling. To this end, we seek to closely investigate this region by accurately measuring temperature profiles through the canopy at a high resolution.

As stated before, temperature gradients become large in the atmospheric region just above the grass. This is due to the fact that the size of turbulent Eddies, which transport heat, decrease when nearing a surface, as their size becomes limited by the distance to the wall. This limitation in turbulent heat transport must be compensated by a steep temperature gradient near the surface.
Formally, heat and momentum profiles over a surface are described by Monin-Obukhov similarity theory (MOST). This theory links vertical gradients of a physical quantity to turbulent fluxes. Profiles that follow from MOST are logarithmic along the vertical, as a result of the aforementioned decrease in Eddy size near the wall. It is well known that MOST is only valid outside of the roughness sublayer (RSL), which is where roughness elements such as grass obstruct and influence flow [3]. In spite of this, these profiles are still commonly used to determine near-surface temperature by extrapolating down to the surface, through the RSL. RSL modifications to MOST have been done for tall canopies [4]. However, extrapolation is still the most common approach for shallow canopies, such as grass [5].

There is an inherent physical inconsistency in the fact that the temperature gradients become infinite at the surface, as a result of the logarithmic nature of MOST profiles. As a consequence, temperatures become undefined at the surface, where z=0. In an attempt to circumvent this problem, the concept of a roughness height is introduced. These parameters are defined for both momentum and heat and are denoted as z_{0m} and z_{0h} respectively. They represent a vertical shift in the logarithmic profiles. z_{0m} is defined to be the height at which the wind speed reaches its surface value. This can rather intuitively be thought of as a no-slip boundary condition. However, for the case of temperature, such an analogy is not as trivial. It is assumed that a similar approach can be taken for heat with the z_{0h} parameter, as for wind. z_{0h} is generally derived from z_{0m}, where the ratio between these parameters is often assumed to be approximately equal to 0.1, from empirical observations. However, this ratio has been shown to differ over multiple orders of magnitude, and is therefore non-trivial to determine and use in models [6]. The determination of z_{0h} remains a prominent source of uncertainty in predicted temperature profiles. Uncertainty in the roughness height results in a significant spread of temperature predictions at higher altitudes. Conversely, when measuring temperatures above the canopy and extrapolating down to the surface, a large spread in surface temperatures is found [7]. See Figure 1.1 for an illustration of this concept.

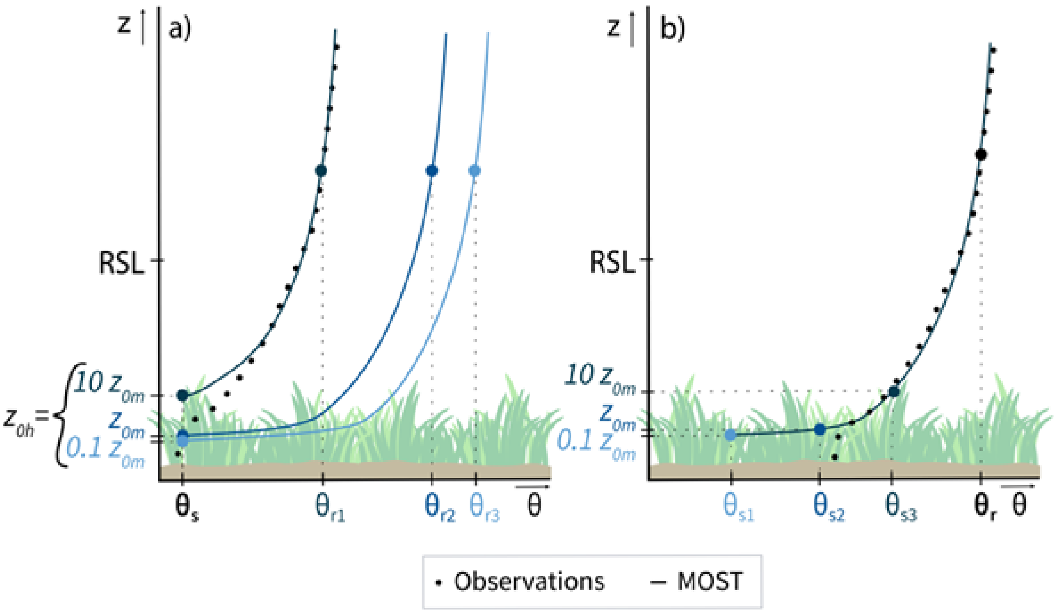

Figure 1.1: This figure is the result of a preceding field campaign, using distributed temperature sensing [8]. The combination of the roughness height concept and the logarithmic nature of MOST profiles causes a high sensitivity to small perturbations in temperature. The left image illustrates the need for non-physical values for z_{0h} to properly match the observed temperature profile above the roughness sublayer. Conversely, the right image illustrates that for a given reference temperature, a small perturbation in z_{0h} results in significant surface temperature differences. [8]

We hypothesize that a significant part of this uncertainty can be attributed to the physical non-robustness of the theory, as indicated by the aforementioned infinite gradient near the surface. As a result, we seek a more physically consistent description of the temperature profiles near the surface. For flow along a smooth wall, such as bare soil, profiles naturally tend towards linear behavior near the wall. This is due to the fact that as Eddy size decreases, viscous transport takes over, resulting in finite gradients near the wall in the so called viscous layer, as illustrated in Figure 1.2. For roughness elements such as grass this becomes much more complex, as the array of grass blades form many individual viscous layers, which are on a much smaller scale than the characteristic turbulent Eddy size. We seek an analogy to this quasi-linear van Driest profile in an effort to more accurately describe profiles near the surface in a physically consistent manner.

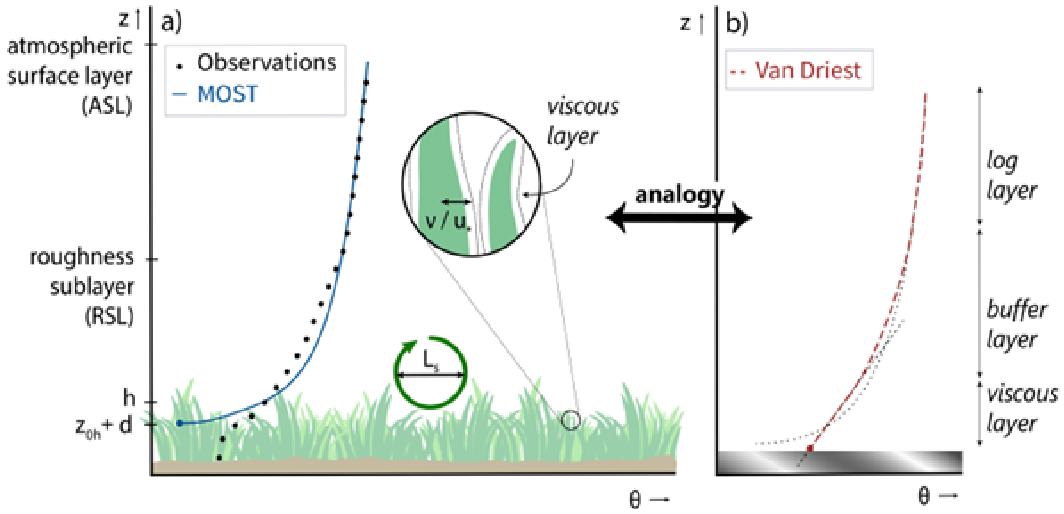

Figure 1.2: The right panel shows a van Driest temperature profile along a smooth wall. Far from the wall, the limiting case converges to the logarithmic shape we find in MOST. Close to the wall the profile shifts to a viscous regime, making it linear. Consequently, the gradient becomes finite at the wall. The left panel depicts the profile over a grass covered rough surface. Here, the interface between the grass blades and the atmosphere form many small viscous layers, at a much smaller scale than the canopy height. The scale difference between the viscous length scale and the surface length scale is illustrated by the round inset and green Eddy, respectively.

More broadly, an important goal for atmospheric modelers is to study the internal canopy dynamics and to unify it with the atmospheric temperature profile. This would allow for a full physical description of temperature profiles from the surface, through the canopy, up into the atmosphere. Reaching this goal was previously impossible, as there was a key element that still lacked in the field of atmospheric science; accurate, high resolution temperature data through the soil-canopy-atmosphere interface is necessary to validate the aforementioned alternatives to MOST. Additionally, a close look into the grass canopy itself is needed to validate models that attempt to describe heat transport within that region [9]. Such campaigns have been conducted before in this context [8] [10] [11], which yielded preliminary results. However, due to uncertainty in vertical location and the moderate resolution, a quantitative conclusion on the performance of the different models could not be drawn with certainty. Additionally, the spatial resolution within the canopy was not yet sufficient to study transport dynamics within the grass. The aim of this thesis is to design and implement a measurement campaign to be able to answer the aforementioned research questions in a quantitative manner, as well as opening up the opportunity for studying internal canopy dynamics. To this end, a temperature profile measurement is done on the millimeter scale, through the canopy. Preliminary analysis will be done on the field data to validate its utility and applications. Temperature profiles and their corresponding gradients will be examined to assess whether the data resolution is sufficient for quantitative model comparison.

In this thesis, the underlying theory is outlined, along with alternative physical models for temperature profile modeling in chapter 2. Subsequently, the design process is presented for an experimental setup that aims to quantitatively compare these models in chapter 3. Calibration tests in the lab are presented, along with the full setup used in the field in chapter 4. Results from both the lab and field campaign are presented, analysed and discussed in chapter 5 and chapter 6. Finally, some suggested future research applications of the dataset are presented.

2
Theory

2.1. Transport in the atmosphere

This section is largely inspired by a book on physical transport through the soil-vegetation-atmosphere continuum, by Arnold F. Moene and Jos C. van Dam [3].
Transport of physical quantities in the atmosphere is mainly due to turbulence, which is a much more effective transport mechanism than molecular diffusion. Turbulence mostly takes place at the surface-atmosphere interface as a result of wind shear and surface heating. It follows that this interface is an important region to study in atmospheric physics. The region where there is a noticeable diurnal variation in turbulence is called the atmospheric boundary layer (ABL). Its height ranges from the order of 100 meters at night, to the order of 1km during the day. Within the boundary layer, we can also identify the atmospheric surface layer (ASL), which comprises roughly the lowest 10% of the ABL. The diurnal variation of the ABL is illustrated in Figure 2.1

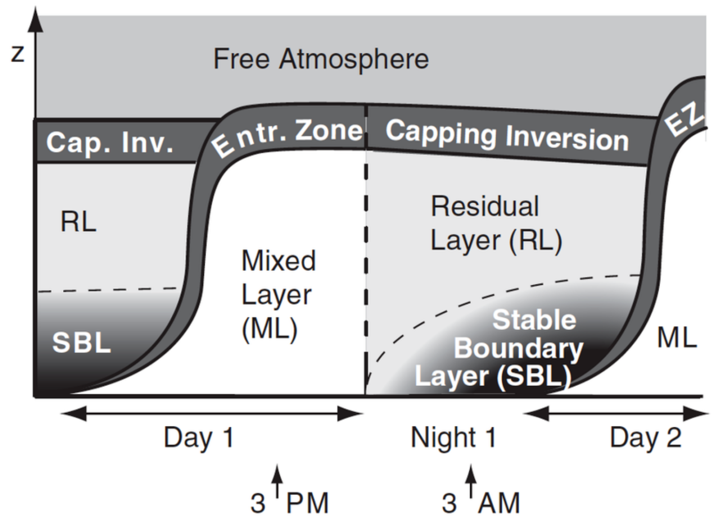

Figure 2.1: The composition of the ABL changes with the diurnal cycle. During the day, there is turbulent mixing as a result of convection from surface heating. As the surface cools at night, the lower part of the atmosphere becomes stably stratified. [12]

Within the ASL, the diffusivities of physical quantities become lower close to the surface. this is due to the fact that the typical size of turbulent Eddies, which transport heat, become smaller when nearing a wall. Therefore larger gradients of mean variables, such as wind, moisture and temperature are needed to transport the same amount of energy. Note that the turbulent flux itself is more or less constant with height at the lowest 20 meters above the soil surface.
The vertical gradients are largely dependent on atmospheric stability, which is in turn determined by the amount of turbulence. Turbulence is quantified by the turbulent kinetic energy (TKE), which is the total kinetic energy of the turbulent motion in every direction. The Richardson number is a parameter

that gives a rough indication of the atmospheric stability, and thus turbulence. It is defined as the ratio of buoyancy production, due to density differences, to shear production, as a result of wind. The flux-Richardson number is defined in Equation 2.1

$$Ri_f = \frac{g}{\theta_v} \frac{\overline{w'\theta_v'}}{\overline{u'w'}\frac{\partial \bar{u}}{\partial z}} \tag{2.1}$$

Here, the flux-richardson number itself is dimensionless, g is the terrestrial acceleration constant [$\frac{m}{s^2}$], $\overline{\theta_v}$ [K] is the average average virtual potential temperature. θ_v' [K], w' [$\frac{m}{s}$] and u' [$\frac{m}{s}$] are the deviations from the mean values of potential temperature, vertical wind and horizontal wind, respectively. The overbar denotes the mean value of these quantities. Finally, $\frac{\partial \bar{u}}{\partial z}$ [$\frac{m}{s}$] is the time averaged vertical gradient of horizontal wind speed.
We can distinguish several conditions on the basis of this dimensionless quantity:

- $Ri_f \approx 0$: Neutral conditions, only shear production of TKE
- $Ri_f < 0$: Unstable conditions, turbulence is produced by both shear and buoyancy
- $Ri_f > 0$: Stable conditions, turbulence is produced by shear, but destroyed by buoyancy

Turbulence at the surface is affected by roughness elements around which the fluid has to flow. In atmospheric physics, these roughness elements make up, but are not limited to: trees, grass and urban structures. These elements are often much larger than the scale of the viscous sublayer for smooth wall flow, which is generally on the order of 1mm[13]. In cases where these obstacles form a semi-homogeneous layer in the horizontal direction, they are referred to as canopies. They can be characterised by their canopy height. The layer in which the roughness of the canopy influences the vertical profiles of physical quantities is called the roughness sublayer (RSL). It is generally approximately equal to 1-2 times the canopy height. [14] [15].
Turbulence in the atmosphere transports physical quantities like heat, momentum and moisture. We take special interest in the vertical transport of these quantities as a result of turbulence. We can describe and quantify this vertical mode of transport by the so-called Eddie-covariance method. This method describes turbulent vertical fluxes in terms of the covariance between the transported quantity and the vertical wind speed. In this thesis, we focus specifically on the transport of heat. For heat transport the relation takes the form of Equation 2.2.

$$H = \bar{\rho} c_p \overline{w'\theta'} \tag{2.2}$$

Here, H is the turbulent heat flux [$\frac{W}{m^2}$], ρ [$\frac{kg}{m^3}$] is the air density and c_p [$\frac{J}{kgK}$] is the air specific heat.
The advantage of The Eddy covariance method is that vertical transport of a quantity can be determined just by measuring the vertical wind velocity and said physical quantity of interest. In the field, a sonic anemometer setup is commonly combined with a high frequency sensor of the variable of interest to determine the Eddy covariance. In atmospheric modeling, we like to model the turbulent flux in terms of gradients of the mean variables. This is referred to as Eddy diffusion theory. This theory is analogous to molecular diffusion. However, in molecular diffusion, the diffusivity is a property of the fluid, while in Eddy diffusion it is a property of flow. Diffusivity is dependent on the intensity of turbulence and, for example, the height above the surface. This makes it non-trivial to mathematically model them in an equation. Historically, based on the development and improvement of the Eddy covariance method, Monin and Obukhov developed their similarity theory in 1954 [16]. This theory could link the turbulent fluxes, as found from the Eddy covariance method, to vertical gradients of a physical quantity of interest.

2.1.1. Monin-Obukhov similarity theory

In meteorological models, we aim to describe the vertical turbulent fluxes of physical variables, such as momentum, heat and moisture, in terms of the mean vertical gradients of the corresponding quantities, like wind, temperature and humidity respectively. In this thesis, we focus specifically on heat.
The link between turbulent fluxes and vertical gradients of physical quantities is especially interesting, as it poses the opportunity for predicting either quantity by measuring the other. However, it is not

always possible or easy to exactly measure the flux of a physical quantity. Therefore, it is useful to link turbulent fluxes to vertical gradients in the corresponding parameter. The mathematical framework that links the turbulent fluxes and the near-surface gradients together is called Monin-Obukhov similarity theory (MOST) and is ubiquitously used in meteorology for the aforementioned purposes. [17].
MOST was derived from dimensional analysis. From the relevant parameters, an expression for the dimensionless gradient is formed. This dimensionless group is subsequently related to a dimensionless turbulent flux, by performing a field experiment [16].
Below, MOST will be explained in detail.
We start with a set of assumptions, which are necessary for the validity of MOST:

- Mean turbulent quantities are stationary in time
- The spatial variation in mean turbulent quantities is only in the vertical direction. I.e. horizontal homogeneity is assumed.
- The mean turbulent quantities are not affected by processes outside of the surface layer.
- The theory is applied outside of the roughness sublayer

The central implication in MOST is that any dimensionless gradient is given by a function that solely depends on $\frac{z}{L}$, where L $[m]$ is a characteristic length scale named the Obukhov length. It is defined as:

$$L \equiv \frac{\overline{\theta_v} u_*^2}{\kappa g \theta_{v*}} \tag{2.3}$$

Here, κ is the dimensionless Von Kármán constant, which is approximately equal to 0.40 and θ_{v*} $[K]$ and u_* $[\frac{m}{s}]$ are characteristic turbulent temperature and velocity scales, defined in Equation 2.5 and Equation 2.4.

$$u_* = \sqrt{\frac{\tau}{\rho}} = \sqrt{-\overline{u'w'}} \tag{2.4}$$

$$\theta_* = -\frac{H}{\bar{\rho} c_p u_*} = -\frac{\overline{w'\theta'}}{u_*} \tag{2.5}$$

Where τ $[\frac{N}{m^2}]$ is a momentum transport parameter, called the surface stress, analogous to the heat flux H.
In the case of temperature (or absolute virtual potential temperature), a flux-gradient relation can be found. This means that that temperature profiles are directly related to the turbulent heat flux. Equation 2.6 gives the MOST relationship between the vertical temperature gradient and the flux as a function of $\frac{z}{L}$

$$\frac{\partial \overline{\theta}}{\partial z} \frac{\kappa z}{\theta_*} = \phi\left(\frac{z}{L}\right) \tag{2.6}$$

ϕ is called the flux gradient profile. In neutral conditions, the flux profile $\phi = 1$ for every relation. This is true by definition, through the choice of the value of the Von Kármán constant. This means that we can find an expression for the temperature gradient in stable conditions, as given in Equation 2.7.

$$\frac{\partial \overline{\theta}}{\partial z} = \frac{\theta_*}{\kappa z} \tag{2.7}$$

using:

$$\begin{cases} \tau = \rho u_*^2 \\ H = -\rho c_p \theta_* u_* \end{cases} . \tag{2.8}$$

The relation can be rewritten to:

$$\begin{cases} \tau = \rho\kappa u_* z\frac{\partial\overline{u}}{\partial z} \\ H = -\rho c_p \kappa u_* z\frac{\partial\overline{\theta}}{\partial z} \end{cases}. \tag{2.9}$$

observe that, in this way, *indeed* a relation between the vertical temperature gradient and the flux is obtained. The relations can be integrated with respect to height, in order to arrive at practical flux-transport laws. These relate vertical fluxes to discrete temperature or wind differences. It is practical to rewrite these relations to the following resistance laws.

$$\begin{cases} \tau = \rho\frac{\overline{u}(z_{u2})-\overline{u}(z_{u1})}{r_{am}} \\ \\ H = -\rho c_p\frac{\overline{\theta}(z_{\theta 2})-\overline{\theta}(z_{\theta 1})}{r_{ah}} \end{cases}. \tag{2.10}$$

For neutral conditions, r_{ah} and r_{am} are identical. We define this aerodynamic resistance as r_a:

$$r_a = \frac{ln\left(\frac{z_2}{z_1}\right)}{\kappa u_*} \tag{2.11}$$

Observe that, indeed, an increase in turbulence as a result of increased wind speeds, represented by u_*, results in a decreased aerodynamic resistance to vertical heat transport.
It is often useful to choose the lower level of temperature observations to be at the surface. However, the asymptotic nature of equation 2.11 makes this impossible, as gradients would become infinite. Additionally, the ground level is located within the roughness sublayer, which invalidates use of MOST completely. Thus, the concept of a roughness height, z_0, is introduced. This height is to be determined from observations. These parameters can be defined for both momentum and heat and are denoted as z_{0m} [m] and z_{0h} [m] respectively. They represent a vertical shift in the logarithmic profiles. z_{0m} is defined to be the height at which the wind speed attains its surface value. It is assumed that a similar approach can be taken for heat with the z_{0h} parameter. $z0h$ is mostly determined from z_{0m} as the ratio between them is assumed to be fixed and approximately equal to 0.1. The roughness height concept is depicted in Figure 2.2.
Filling out z_{0h} and writing out the full equations now gives:

$$T(z) - T_s = \frac{\theta_*}{\kappa} ln\left(\frac{z}{z_{0h}}\right) \tag{2.12}$$

Even with the introduction of the roughness height concept, the gradient of the MOST profile does not become finite at the ground surface, making it an inherently nonphysical model. In reality, near-surface gradients are finite. This leads us to look for other models with a more physically rigorous behaviour near the surface, such as an analogy to the van Driest flow profile for smooth walls, as depicted in Figure 1.2. Below, some adapted models are outlined.

2.1.2. Alternative models

One model developed by Paul Nollen, coined **the z plus b model**, introduces a shift in the z parameter, which changes the model such that the gradient converges to a finite value [18]. The relation is then given in stable conditions as

$$\frac{\partial\theta}{\partial z} = \frac{\theta_*}{\kappa(z+b)} \tag{2.13}$$

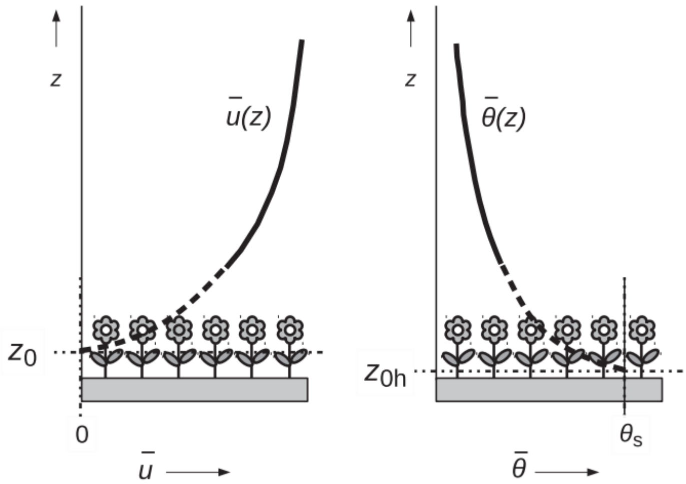

Figure 2.2: The concept of a displacement height can be introduced, both for wind velocity and temperature profiles. They are denoted as z_{0m} and z_{0h} respectively. The introduction of this variable shifts profiles along the vertical coordinate in such a way that the bottom of the extrapolated profiles attain their surface values. Note that the dashed line indicates the fact that the MOST profiles are extrapolated down into the RSL, which is a region where it is not valid.[3]

This expression for the temperature gradient is analogous to the MOST gradient given in Equation 2.7, with the addition of a translation of the z coordinate. This allows the gradient to shift vertically, adding a new degree of freedom to the model. In the limiting case where we near the surface, z becomes very small. In the expression, this means that the temperature gradient asymptotically approaches a value of $\frac{\theta_*}{\kappa b}$. This finite limit in the temperature gradient is a more physical result in comparison to MOST. κb has a physical interpretation in the fact that it represents a finite length scale, analogous to the z_{0h} concept, which is now determined by the structure of the surface.

Another way of ensuring the gradient converges to a finite value at the surface is by introducing a quasi-viscous term into the calculation of the friction velocity [19] [20], called **the adapted van Driest model**. It is an adapted version of the van Driest model for momentum transport in smooth channel flow [21]. This model introduced a buffer layer, which represented a gradual decrease in Eddy diffusivity when nearing the wall, rather than a discrete transition between the logarithmic and viscous layers. In the van Driest model, the Eddy diffusivity is gradually decreased by an exponential damping function. The adapted van Driest model adds a stability correction to this concept [19]. This results in a reformulation of the friction velocity along a smooth wall, given in Equation 2.14.

$$u_*^2 = \left[\frac{(A\kappa z)^2}{(1+\alpha\frac{z}{l})^2}\frac{\partial U}{\partial z} + \nu\right]\frac{\partial U}{\partial z} \tag{2.14}$$

Here, A is a dimensionless exponential damping function, alpha is a dimensionless, empirical parameter $\alpha \approx 3.5$, and ν [$\frac{m^2}{s}$] is the kinematic viscosity.
Dividing both sides of Equation 2.14 by u_*, a length scale appears, given as $\frac{\nu}{u_*}$ [m]. To arrive at an analogy for temperature profiles through grass, rather than for smooth surfaces, we replace the viscous parameter with the concept of an eddy viscosity: ν_t [$\frac{m^2}{s}$]. For brevity, we immediately substitute the new turbulent length scale by introducing the L_s [m] parameter, which is analogous to κb in the 'z plus b' model. This is a length scale which serves an analogous purpose to the viscosity in the case of flow along a smooth wall. However, this parameter is determined by the surface geometry, rather than the fluid itself. Combining this result with Equation 2.6 results in a new relation for the temperature gradient, given in Equation 2.15 [19][20].

$$\theta_* = \left[\frac{(A\kappa z)^2}{\theta_*(1+\alpha\frac{z}{l})^2} \frac{\partial\theta}{\partial z} + L_s \right] \frac{\partial\theta}{\partial z} \tag{2.15}$$

Note that this formulation results in a finite gradient near the surface. Furthermore, in the high z limit, the relation converges back to the traditional MOST description, as is desired from an alternative model. Furthermore, note that solving the temperature profile from this relation is not possible analytically, and therefore requires numerical integration techniques.

2.2. Distributed temperature sensing

Distributed temperature sensing (DTS) is a method that allows temperature measurements over very long distances, on the order of $10^3 m$, at a resolution on the order of $10^{-2} m$. The method is therefore well suited for a large range of applications, both in large surface surveying and very high-accuracy localized measurements.

2.2.1. Raman scattering

Raman scattering occurs when photons scatter inelastically within a medium. This scattering event yields either an increase, or decrease in photon energy. the former is referred to as Anti-Stokes scattering, while the latter is called Stokes scattering. [22]
Light travelling through a fiber-optic cable will scatter as a result of imhomogeneities within the cable. Most abundantly, these will be elastic scattering events, also referred to as Rayleigh scattering. However, a small portion of these events will undergo the aforementioned Raman scattering. The frequency of both Stokes and Anti-Stokes scattering events are influenced by the temperature of the medium. The degree to which the the frequency of the scattering events changes is different for Stokes and anti-Stokes scattering. Therefore, by measuring the intensity of both scatter peaks at a reference temperature, information about the temperature elsewhere in a fiber-optic cable can be attained.

2.2.2. DTS systems

In practical applications a laser will shoot a pulse of light with a known wavelength into a glass fiber cable. Upon scattering, a photon will return towards the start of the cable, where the energy can be measured. Repeating this process a multitude of times will result in energy spectra with two clearly identifiable Raman shifted peaks. These correspond to the Stokes and Anti-Stokes scattering events. One spectrum will emerge for every measurement point along the fiber, the spatial resolution of which is determined by the Gaussian distribution of time-of-flight measurements. Sections of cable are kept at a known calibration temperature to get reference information. This yields localized temperature information along a fiber optic cable, which forms the principle behind the DTS method.

Off-the-shelf devices exist that perform the measurements described before. These devices are widely used in the environmental sector, as they supply large-scale temperature measurements, at an accuracy of 0.1 K, a on a sub-meter resolution. [23]

DTS devices can be set up such that both ends of the fiber are used. In such a double-ended configuration the device alternates between two measurement channels that send pulses from both ends. The advantage of this is that the effects of exponential intensity decay can be compensated for, in addition to overcoming the effects of large step losses which may occur due to damage to the cable. It is therefore always recommended to configure a DTS into a double ended setup. [24]
It is possible to use DTS as a proxy to measure local air temperature. However there are several factors that should be taken into account when attempting this. Firstly, the fiber absorbs solar radiation which in turn heats it beyond the ambient air temperature, resulting in an offset towards higher temperatures. This perturbation has been studied and can, to a certain degree, be corrected for [25] [26]. Secondly, evaporation has a significant cooling effect on DTS fibers, as is extensively documented and even used for measurement of wind speed [27] [28]. The assumption that is made when when measuring air temperatures using a DTS setup is that the fiber is in thermal equilibrium with the ambient air, which

is not always the case as a result of these factors.

The DTS method will form the basis for the experimental setup that will be used in the field experiment. In the following chapter, the aforementioned aspects will be incorporated into a design process from which the final experimental setup will follow.

3 Setup design

We aim to tackle the challenge of measuring temperature profiles through grass at a very high accuracy and resolution. Generating such data had previously not been possible. However, with the advancement of novel measurement techniques, such as DTS, we can take an unprecedented closer look near the canopy. To tackle this challenge, a design is to be formulated to pass all essential criteria to yield the desired dataset. This chapter outlines the full design process to arrive at this solution. The final result of this process is presented in section 3.4.

3.1. Design analysis

3.1.1. Problem statement

In the former chapter, the conventional theory to describe near-surface temperature profiles was discussed. We aim to investigate the accuracy of this description just above the grass. To this end, there is a need for high precision temperature observation, on the millimeter scale.
A measurement setup is to be designed that can give a proxy for air temperature along the vertical coordinate. This setup will be placed in the field at the Cabauw observatory for several weeks to collect data.
The requirements for this setup are compiled into a set of criteria that need to be passed to yield successful data. These consist of main criteria, such as the measurement resolution and some practical constraints, such as field conditions. They are presented in subsection 3.1.2
Findings from similar campaigns that preceded this one are taken into account in the design process [8] [28] [10] [11], either explicitly as criteria, or implicitly during synthesis.

3.1.2. Criteria

- The device will have to measure a vertical temperature profile, at an accuracy of at least 0.1 $^{\circ}C$, spatial resolution of at least 5 mm, and a time resolution on the order of 1 minute. Note that high-frequency temperature fluctuation due to turbulence itself are beyond the scope of this campaign
- The design must accommodate the adaptation of physical dimensions, such as height, width, or other physical parameters, such that a wide range of setups can be realised, without the need for redesign in future campaigns. This also allows for quick iteration when prototyping
- The measurement must be representative for a local observation: There should be no further spread than 0.5 m in both the x and y direction, to ensure sufficient homogeneity to extrapolate the vertical gradient.
- The measurement must be representative of local air temperature: The sensor itself must have a minimal thermal mass and maximized thermal conductivity to closely follow the ambient air temperature. Any auxiliary parts, such as a frame, must minimize both parameters to avoid thermally influencing the sensor. See subsection 3.2.2 for a definition and explanation of these parameters.

- The device must have as little influence on the local environment as possible:
  - The design should absorb as little radiation as possible, both in the long wave and short wave regimes
  - The air permeability of the device has to be maximized, to let air flow through it with the least influence on the ambient air flow.
- The design needs to be easily and consistently reproducible to be able to verify measurements
- The design must be fabricated using commonly accessible materials and tools. This includes all materials that can be delivered from an online supplier. The most common manufacturing methods are included: commonly accessible manual power tools, 3D printing, laser cutting, CNC milling
- The sensor used for the design must either already be available or within the budget of the Geoscience and Remote Sensing (GRS) group at the TU Delft
- The device must be able to withstand Dutch weather extremes for at least 3 months in the field during springtime. For this full period it must:
  - Withstand temperatures between 0 and 25 $°C$ [29]
  - Withstand windspeeds of up to 20 m/s [30]
  - Withstand daily solar radiation of up to 1200 W/m^2 [31]
  - Be fully water resistant, i.e: remain undamaged when fully submerged in water, as heavy rainfall is common in the field. [32]

3.2. Synthesis

In this phase, possible solutions to the design problem are outlined. The design will be based on the DTS method. In this section the shape of the frame that will hold the fiber is synthesized. Subsequently, an appropriate material will be selected.

3.2.1. Shape design

Two main branches of physical form design were explored in this phase. The number of designs was kept limited at this stage, as a result of the possibility for rapid prototyping to test ideas, making many design iterations possible.
Firstly a design was made for a **3D printed helical structure**. The fiber would be clamped into the rim of an aerodynamically streamlined profile, which would spiral vertically up. The spiral would be supported by regularly interspaced support struts with the same cross-sectional profile. The design is depicted in Figure 3.1. It bears many similarities to the ground screw design by Bart Schilperoort [33].
Another potential physical form for the frame is a **ring supported rib structure**, between which the fibers are suspended under tension. Such a design can be realized in a laser cutter, achieving a 0.1 mm accuracy on fiber placement. The fiber will mostly be in contact with the surrounding air and only contact the frame on the contact points with the ribs. Additionally, the frame is permeable to airflow. An initial impression of this structure is depicted in Figure 3.2
Both of these designs were taken to the simulation stage in the form of a digital 3D design to assess their viability. The 3D printed design quickly proved impractical for several reasons. Firstly, printing the structure itself would be a challenge, as a result of the multitude of overhangs. This would require significant amounts of print supports, which can be difficult to remove entirely, especially to a point where the surface can be considered aerodynamically smooth. Furthermore, the cable is in contact with the frame at every location. This means that only half of the cable is exposed to the ambient air at any point. As a consequence, the frame has a very significant impact on the measured temperature, which is problematic if temperatures change quickly. The design of the similar ground screw, by Bart Schilperoort, has no such limitation as the thermal inertia of soil is much larger than that of air, in addition to the fact that heat transport in this region is limited by thermal conduction.
In comparison, the latter proposed rib-based design evidently scores better on many important criteria, such as ease of fabrication, minimized fiber contact and thermal mass. The simulated 3D model does not appear to reveal any unforeseen issues with the design. Therefore, this shape design is chosen for subsequent design steps.

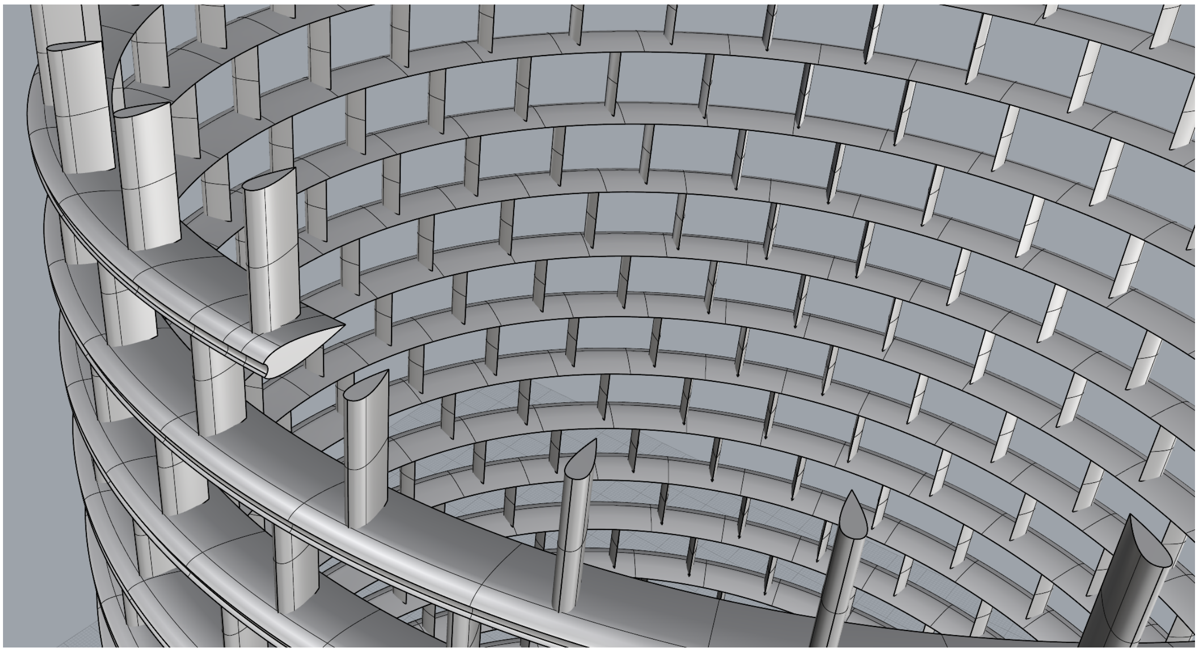

Figure 3.1: A computer generated design of the 3D printed design.

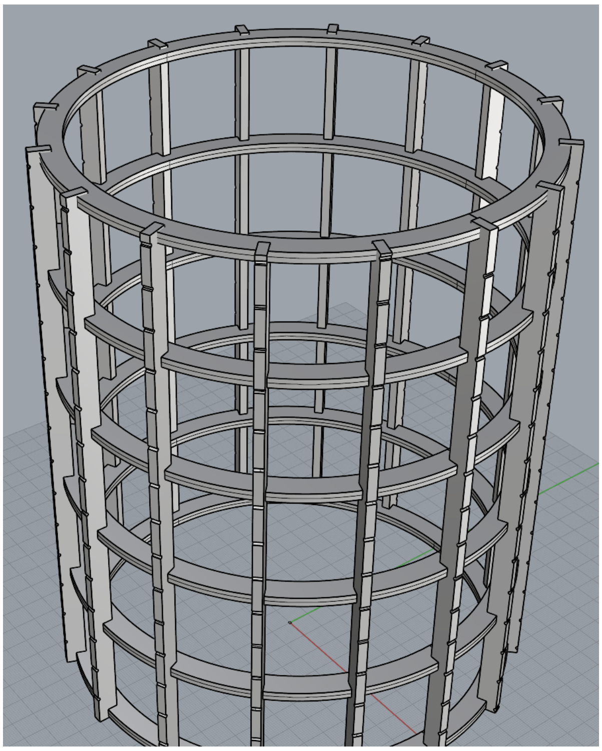

Figure 3.2: A computer generated design of the initial lasercut rib structure design.

3.2.2. Material analysis
A material choice will have to be made regarding the frame material. When selecting a proper material it is crucial to keep the initial criteria in mind.

The selection process is constrained by several pass-fail criteria, along with an optimization criterion; the frame should have the lowest possible thermal influence on the fiber. Primarily, this hinges on thermal mass of the frame, which indicates the amount of heat the frame material can store on a volumetric

basis. It is defined as the product of material density and specific heat: $\rho c[\frac{J}{m^3 K}]$. This parameter ought to be minimized in this optimization.
Secondly, the thermal conductivity $\lambda[\frac{W}{mK}]$ is an important factor that determines how quickly the frame can transfer heat to the fiber. For conduction between two isothermal planes, it is defined as: $\lambda = \frac{Qd}{A\Delta T}$, where $Q\,[W]$ is the amount of heat transferred, $d\,[m]$ the distance between the isothermal planes, $A\,[m^2]$ the area of the surface and $\Delta T\,[K]$ the temperature difference. This parameter should be also be minimized in this optimization, to ensure the lowest amount of heat transfer between the frame and the fiber.

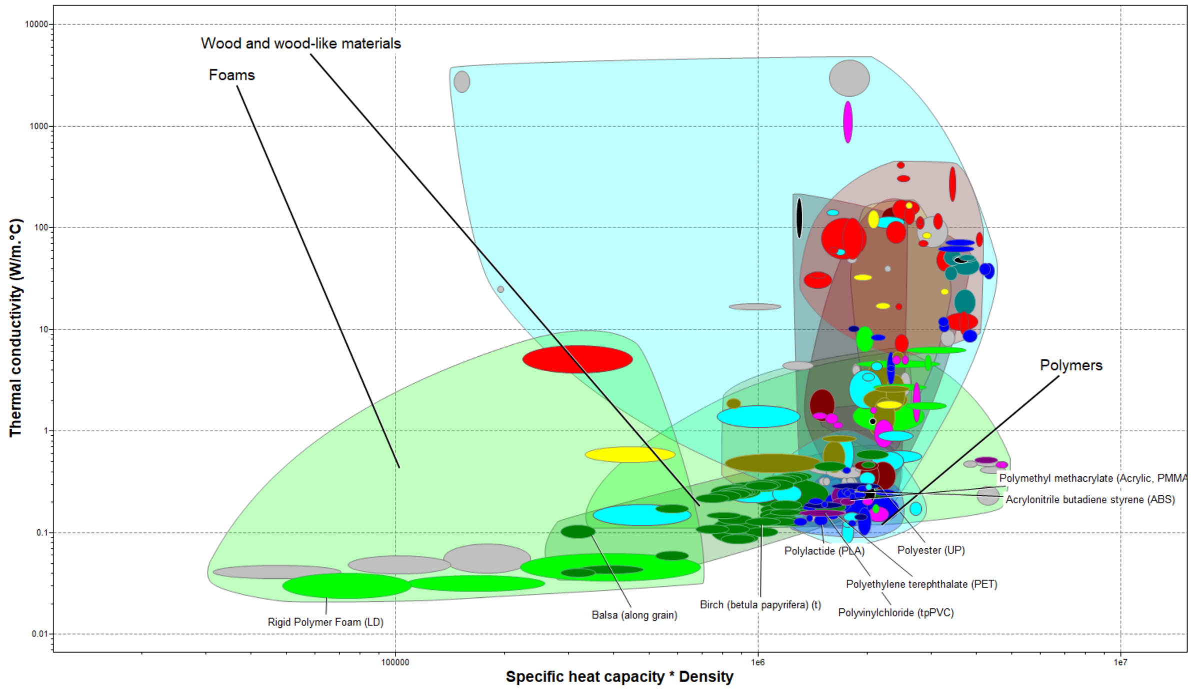

Figure 3.3: An Ashby plot depicting the optimization parameters for several material families [34]. The thermal conductivity and thermal mass of materials are plotted on logarithmic axes. According to the optimization criterion, the bottom left of the figure represents the region with the most advantageous thermal characteristics.

To select a material against a set of parameters that are to be optimized, an Ashby plot can be used, as shown in Figure 3.3. Material group properties are plotted on a logarithmic axis to visually represent the most suitable materials. This figure contains a broad range of material families. Not all of the suggested materials are suitable, keeping in mind the aforementioned pass-fail criteria. To optimize both thermal conductivity and thermal mass, we strive for materials in the bottom left section of the figure.
The material group which has the most advantageous, minimized thermal conductance and thermal mass is the foam material family. While it has desirable thermal properties, it lacks in rigidity and resilience against moisture. Additionally, it is not easily processed or shaped in a reproducible manner. This makes the material group unsuitable for the intended application.
Wood is the second group with desirable thermal properties. These materials, in contrast to foams, have sufficient rigidity to form a robust frame. Wood is also easily and accurately processed by various methods, most notably laser cutting. However, wood is notoriously prone to damage and warping as a result of moisture, which compromises the structure of the frame and may cause shifting of the fiber. The wood would have to be covered by a secondary protective layer, which would negatively affect the accuracy of the fiber position. Furthermore, the thermal properties of such a layer would likely be unknown, possibly making the solution much less advantageous.
Polymers form the third best suited material group. Here we find many different commercially available polymer types. One of the materials contained in this group is polymethylacrylate (PMMA). This material has several notable desirable properties. The material is widely available in sheets of several colours, which can be precisely processed using a laser cutter or a CNC mill, making it very accessible to work

with. Furthermore, the material is rigid, waterproof and UV resistant. The material passes all the pass-fail criteria, while having a minimal thermal mass and conductivity.
We therefore opt for sheets of high-gloss, white PMMA, which will be processed using the laser cutter to fabricate the design.

3.3. Iterative simulations

In order to simulate the resulting frame and test it against some of the specified criteria, several prototypes were fabricated. To this end, a universal lasercut file (svg) generation program was made in grasshopper [35] to create files, based on physical parameters that can be adapted for different use cases. more information about the file generator, including the source file can be found in Appendix A.
The initial design as formulated in subsection 3.2.1 was taken into a second round of simulation. It was physically constructed out of MDF to test the structural properties of the frame. The result is depicted in 3.4

Figure 3.4: The first prototype of the initial design for the frame made out of MDF. it features circular support rings, held together by vertical struts. Thread is used to simulate the glass fiber cable.

The subsequent evaluation step concluded that the frame was structurally sound and kept the fiber in place. However, the frame was influencing the fiber by having unnecessary points of contact at the support rings. This would likely introduce a significant bias in the measurements where the support rings are. Based on this fact, the decision was made to iterate back to the synthesis phase. Here, the rings were moved further back toward the center of the coil. In addition to that, the supports were made polygonal, such that the path of the fiber would be followed.
The initial frame has no way of being properly secured to the surface. Successive versions were fitted with stakes at the bottom, which make sure the frame is firmly embedded in the soil.
From the iteration to the synthesis step, the design was again simulated. The fabricated design is depicted in Figure 3.5

Figure 3.5: the iterated design of the coil, made out of MDF. the coil now features polygonal support rings, such that the shape of the glass fiber is followed. Additionally, the fiber is tensioned using Lester terminals at the start and end of the coil. Small stakes were included at the bottom for embedding it in the soil.

3.4. Final decision and design

After the final iteration, the design is found to pass all criteria that pertain the physical shape of the coil. The fiber is kept firmly in place by the frame, resulting in a very well defined position. The frame is sufficiently rigid to all stresses, with the exception of torsional stress. This can be effectively counteracted by anchoring the top of the coil to the ground at 4 vertices. This can be done in a non-intrusive way by using thin nylon wire. This rigidity, in combination with the specifications of the DTS machine will yield the desired resolution and accuracy.
The final design will be fabricated from reflective, white PMMA, as determined in subsection 3.2.2. This material passes all criteria as it's UV resilient, waterproof and sufficiently strong.
The fact that the design is lasercut from a generated file makes it well reproducible and adaptable. This way the vertical resolution can be tweaked to the desired value. For the setup at Cabauw the parameters are given in Table 3.1

Coil parameters	**Value**
Coil radius	159.155 mm
Coil height	1000 mm
Winding resolution	0.2 turns/mm
Fiber diameter	1.6 mm
Number of support ribs	10
Number of support rings	6

Table 3.1: Physical design parameters for the Cabauw setup

The fabricated final design is depicted in Figure 3.6. This leads us into the final simulation phase, where the coil is tested under several conditions in the lab. The description and results of this setup are presented in section 4.1 and 5.1.

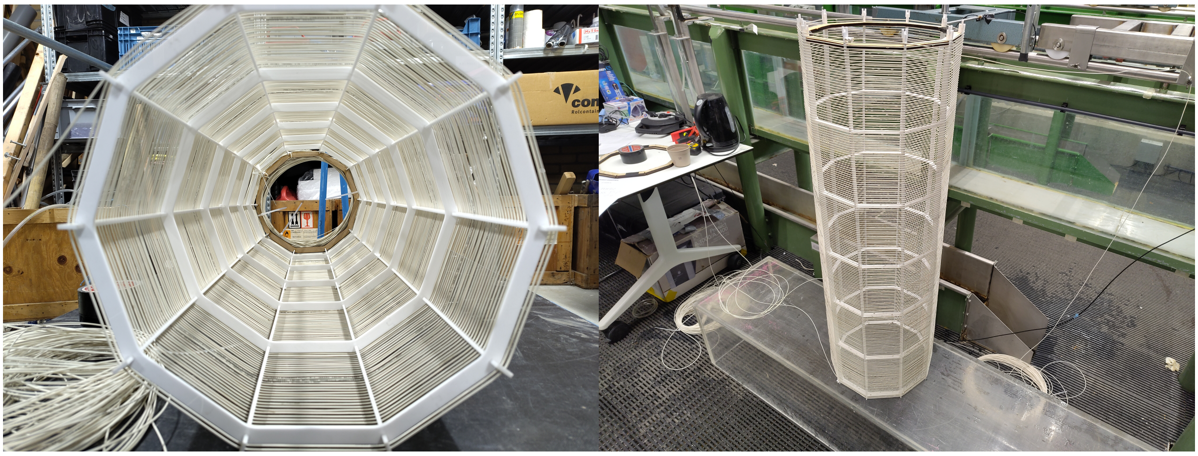

Figure 3.6: The final design of the coil. It is a PMMA frame, which keeps the fiber at a fixed location by tension on the support ribs. The fiber is kept tensioned by luster terminals at the start and end of the coil. The bottom of the coil has attachment points for long stakes, which will be driven into the ground when installing it in the field.

4

Experimental method

4.1. Coil lab testing

The coil was extensively tested before being installed in the field at Cabauw to study responses to environmental factors in an isolated manner. Several conditions were tested.

4.1.1. Vertical resolution

To test the vertical resolution of the coil, it was subjected to a strong temperature gradient, which moved along the length of the coil at a constant rate. The coil was positioned in an empty cylindrical container which was slowly filled up with cooled water. The cool water was sourced from a reservoir with ice, which was at a temperature of approximately 10 °C. The water was siphoned into the bottom of the container to slowly get the cold water level to rise at a constant rate. Air and bath temperatures were monitored using PT100 temperature sensors for reference. The setup is shown midway through the measurement in Figure 4.1.

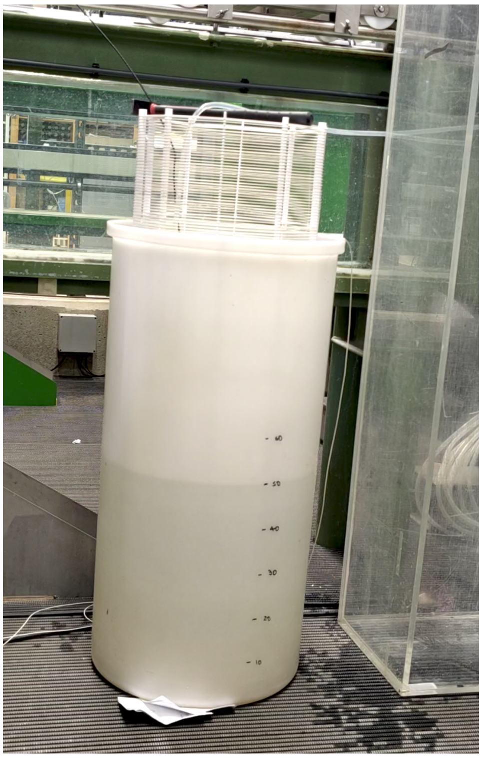

Figure 4.1: The setup for the determination of vertical resolution; The coil is placed in a vertical container as cold ice water is siphoned into it, making the water level rise slowly over time. This creates a moving temperature gradient along the coil.

4.1.2. Horizontal localization

A very similar experiment was conducted to examine the possibility of horizontal localization and to study the effect of temperature gradients in the horizontal plane. The coil was submerged in cool water with a similar setup to the vertical case, though now in a horizontal container. The water level was again raised at a steady rate over time. Both the ambient air and reservoir were monitored using the PT100 sensors. The setup is depicted in Figure 4.2.

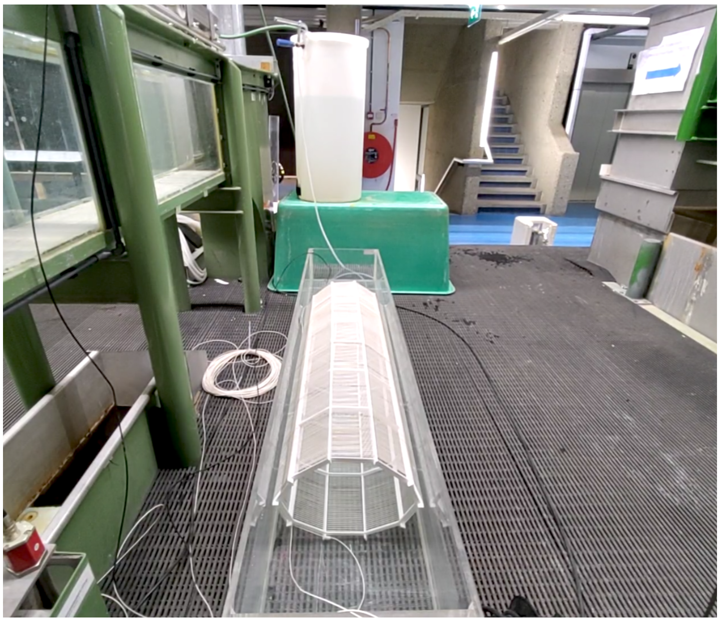

Figure 4.2: To evaluate horizontal localization possibilities, a similar approach to Figure 4.1 was taken. Now the coil is submerged in a horizontal tank.

4.1.3. Precipitation

As precipitation and moisture are common in the field, the effects of wetting the coil were examined. To this end, the coil was fully submerged in a cylindrical container, taken out and left to dry over a long period, giving an indication of drying time without the effects of wind. The coil was put on top of a platform in an attempt to minimize the effect of the ground surface. Furthermore, the PT100's were both set up in in air at the top and bottom of the coil respectively for reference.

4.1.4. Convection

Studying the effects of heated, forced convection on the coil gives an indication of its permeability to wind. An experiment was done where the coil was heated with a hot flow of air in the center. A hair dryer was used for this purpose. The setup is shown in Figure 4.3.

4.1.5. Radiation

Finally, the effects of radiation were examined in the lab. Mimicking the full solar spectrum and radiative power in isolation from other factors was neither practical nor necessary. The aim is to study the effects of long wave radiation in reference to the rest of the coil, to identify artifacts that arise from it. To achieve this, an experiment was conducted where a 2kW heat lamp was pointed at the coil, which generates exclusively long wave radiation. Half of the coil was shielded from radiation to be able to study both regimes. The setup used for this is shown in Figure 4.4.

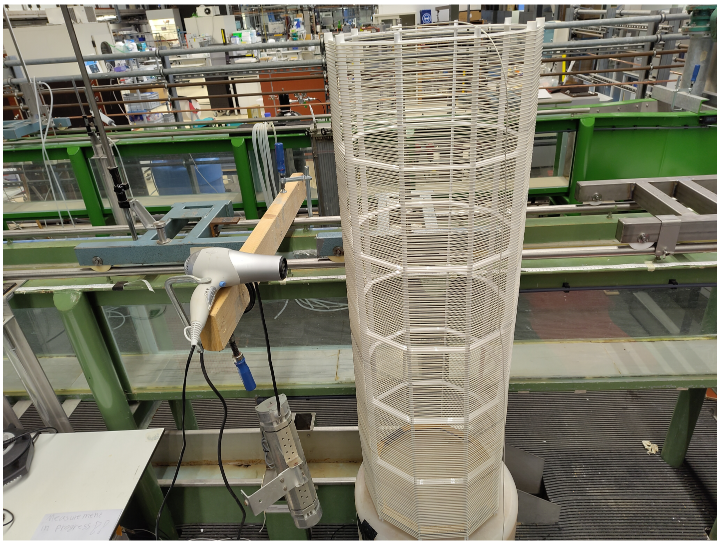

Figure 4.3: The setup for heated, forced convection

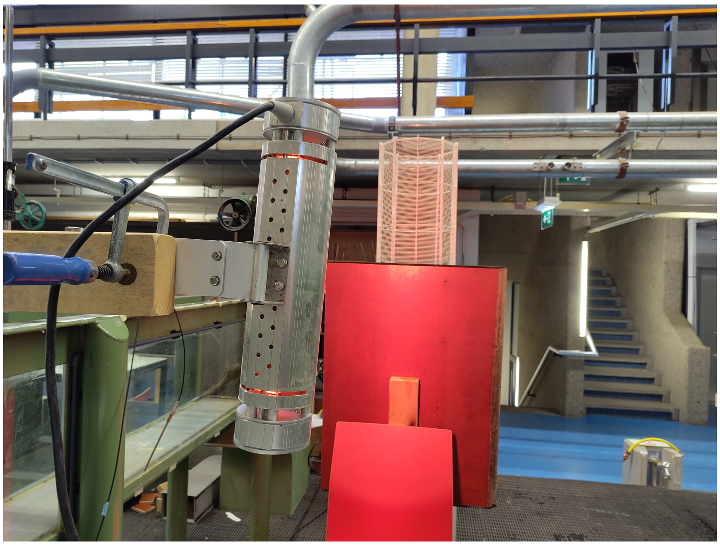

Figure 4.4: The setup for measuring radiation effects. A 2kW heat lamp is positioned in front of the coil. The bottom section of the coil is shielded, while the top part is exposed to the radiation.

4.2. Field experiment setup overview

After the experiments in the lab, the results of which are presented in chapter 5, the setup is installed in the field. This section describes the arrangement for the field experiment.

The field experiment is set up at the Cabauw observatory [36]. This is a meteorological observation site, situated in a polder near Utrecht in the Netherlands (51.971° N, 4.927° E). It is operated and maintained by the royal Dutch meteorological institute (KNMI). The site is well suited for observations as it is located in a relatively undisturbed, mostly agricultural area. Many research campaigns are conducted at Cabauw for this reason [37].
The field experiment features three distinct sections, which measure temperature over several ranges. In addition to the coil that was designed in chapter 3, a ground screw and a 5 meter mast were included in the setup. The former extends the profile 25cm down into the soil and the latter extends it upwards by 4 additional meters into the atmosphere. These sections have partial overlap, which allows for validation and extension of the individual profiles. The sections will be linked together via splices, which require calibration in baths of water, kept at a known temperature. The ends of this loop end up at

the data acquisition cabinet, where the DTS and power supply are located, among other necessary equipment.
From the central data acquisition cabinet, the glass fiber cable is run through a hot and a cold calibration bath, indicated in red and blue respectively. After every set of calibration baths, the fiber is run to one of the sections, after which it is returned through the baths to be spliced to the next section. Calibration is necessary after every splice, resulting in a total of 6 passes through the baths. The schematic representation of which can be found in Figure 4.5

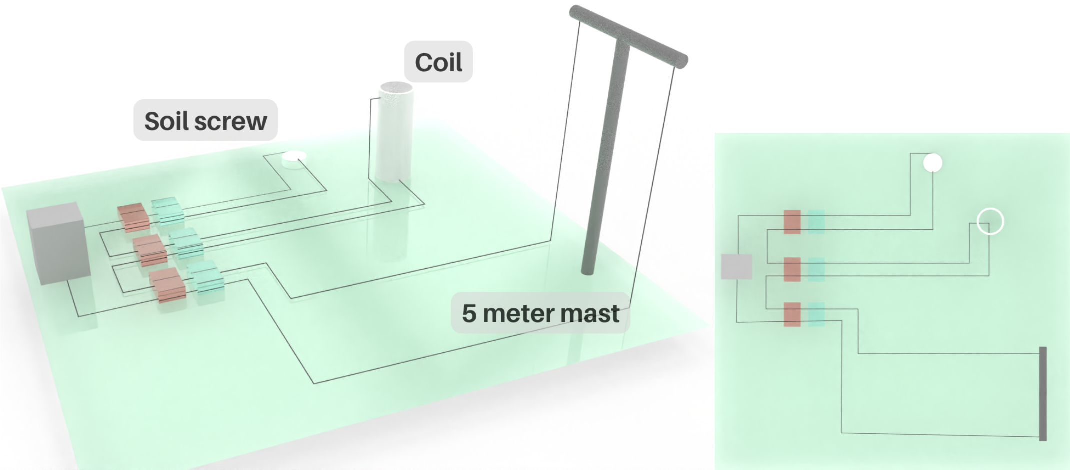

(a) overall view **(b)** Top view

Figure 4.5: Schematic showing the full setup that will be placed at Cabauw. The data acquisition cabinet is depicted in grey to the left side of the figure. Hot and cold calibration baths are indicated in red and blue, respectively. The three measurement sections are shown on the right

4.3. Data acquisition cabinet

A server cabinet was used to house all the electronic equipment for the data acquisition 4.6.
Starting at the bottom of the cabinet, the uninterruptible power supply (UPS) is depicted, which is used to power the DTS. In case of power grid failure, its battery will supply the DTS with sufficient power to safely shut down the system to prevent damage. On top of the UPS there is a hard drive (red), which is where the DTS directly writes all of its data. Behind the hard drive there is a white breadboard with a bmp280 sensor which was used to log temperature and humidity within the cabinet, to validate proper operating conditions for the equipment inside. The DTS was placed on the middle shelf. At the top right of the DTS two fiberglass cables emerge for the double ended measurement. The PT100 probes are connected in the middle section for use in the calibration baths. On top of the DTS is the monitor for operating the machine. Finally, to the top left of the cabinet there is a bag of dehumidifying salts to keep moisture levels low within the cabinet.

4.4. Calibration baths

To accurately measure temperature, the raw signal from the DTS has to be calibrated against a section with a known temperature. Furthermore, splicing fiberglass cable together will result in signal loss. This means that every splice requires a recalibration of the temperature in the fiber. Calibration baths are used for this purpose. These baths are filled with water, such that they have a high thermal inertia. One of the baths is heated to a constant temperature by means of an aquarium heater, while a pump ensures proper mixing, as shown in Figure 4.7.
The other bath remains unheated and unmixed. The baths are insulated by a layer of foam and are sealed at the top. Every time the cable is passed through a bath it is coiled up to lengths of approximately 10 meters. This ensures that there is enough signal with a known temperature to calibrate against.

Figure 4.6: The inside of the data acquisition cabinet

Figure 4.7: The inside of the heated calibration bath

4.5. Coil

An MDF template (Figure 4.8) is used to accurately pre-drill the locations of the stakes for the coil. These holes are then fitted with pre-cut stakes, which are also made of PMMA. The coil is then placed on top of these stakes and is glued to ensure rigidity. Additionally, the coil is tethered at the top in the 4 cardinal directions for further structural integrity. This is done using transparent 0.5mm nylon wire to minimize influence on the measurement.

(a) The template used to drive the stakes in.

(b) The stakes being driven into the soil after using the template.

(c) The coil is glued onto the stakes.

(d) The coil is tethered to the ground using 0.5mm nylon wire.

Figure 4.8: This figure depicts the process of installing and securing the coil in the field.

4.6. Ground screw

For the general overview, extending the measured profile down into the soil is advantageous when analysing the data. The temperature profiles can then be extrapolated and used to validate the coil measurements. Note that this approach is unique in atmospheric literature. With this approach, the full soil-vegetation-atmosphere continuum temperature profile is documented at a mm-cm resolution. To measure the temperature profile into the soil, a ground screw was used [33]. This design has been extensively tested, with successful results. Therefore it can be installed as an off-the-shelf module, where no further design is required.

The screw needs to be fabricated from individually 3D printed parts. The glass fiber cable is fed through the input of the screw, keeping a margin of $\pm$ 100 m at both ends for calibration and splicing. The fiber is then wound onto the screw by pushing it into the grooves, making sure not to cause any breakage. Once the full screw is wound, the 3D printed parts are glued together and the inner cavity is filled with PU foam to avoid convective transport within the screw. The screw is depicted in Figure 4.9

(a) Winding of the ground screw with the glass fiber cable **(b)** Installed screw in the field

Figure 4.9: The ground screw by Schilperoort et al. [33] as used in the field campaign

Once in the field, a hole of 70 mm $\varnothing$ is drilled into the soil using an auger. The screw can then be screwed into the hole, until the top is flush to the surface of the soil.

4.7. 5m mast

For the aforementioned reason of extending the measured data, a 5m mast is included in the setup. This allows for extension of the temperature profiles higher into the atmosphere.
A mast was designed to take the fiber straight up and down again over a vertical distance of 5m. This section is not wound, resulting in a significantly lower vertical resolution of approximately 25cm along the vertical. The mast is made from modular scaffolding pipes and connectors, to allow for adaptation in future campaigns. The fiber is clamped at the bottom by a combination on insulation tubing and hose clamps. The fiber is guided by pulleys at the top of the mast, so as to keep bending radii large enough to prevent breakage or significant signal losses. The mast is depicted in Figure 4.10

Figure 4.10: The 5 meter mast placed in the field

5

Results

5.1. Coil lab calibration

The coil was extensively tested under lab conditions to determine its properties in a controlled environment. Several conditions were simulated and analysed. This data is essential to determine whether all criteria postulated in subsection 3.1.2 have been met, for example with respect to the resolution. Additionally, it is useful to know to what extent the signal is disturbed by radiative effects or wetting after precipitation. These factors play an important role in the field. When these conditions can be isolated from other variables in a lab environment, field data can be filtered accordingly.

5.1.1. Vertical resolution

The vertical resolution of the coil was determined by submerging the coil in a vertical container with chilled water. The water level was slowly increased at a constant rate, such that a steep gradient was measured at the water-air interface. This gradient was tracked over time, which allows for determining the vertical resolution. In Figure 5.1 the Temperature data from this experiment are visualized over time. In this figure, a clear interface can be identified, where a strong gradient is present.

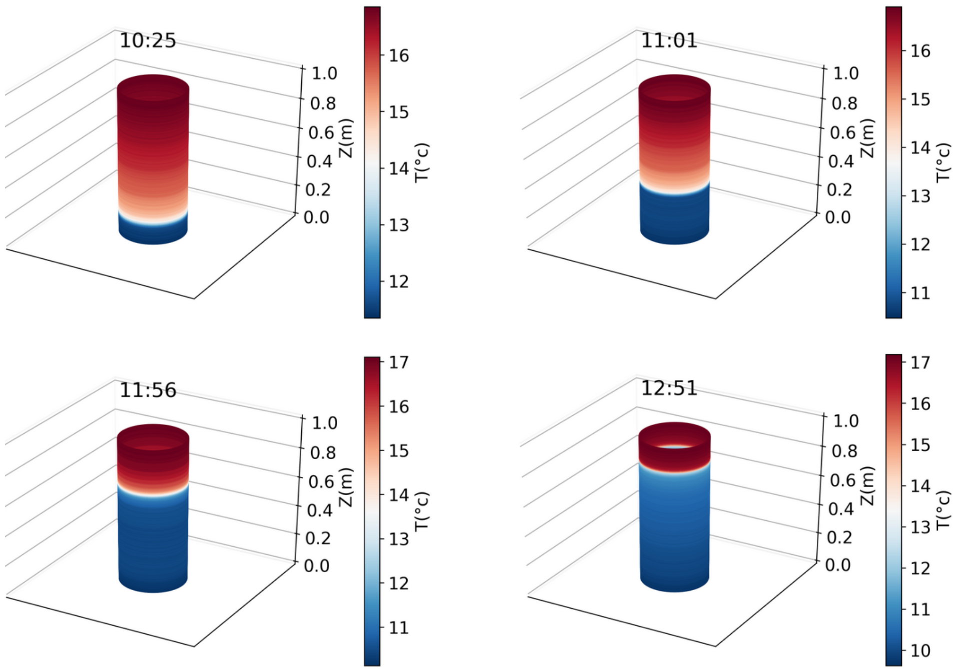

Figure 5.1: The temperature data is projected onto a cylinder to illustrate the displacement of the temperature gradient over time. The increase of the cold water level can clearly be observed over time, as indicated at the top of the subfigures.

For every timestep, the maximum gradient was localized along the length of the fiber and plotted over time, as shown in Figure 5.2. This shows a clear change in the air-water interface level which is linear over time. As the water level was constantly rising over time at a known rate, information about the setup accuracy can be extracted by comparing the measurements to the line describing the water level change. This process is depicted in Figure 5.3.

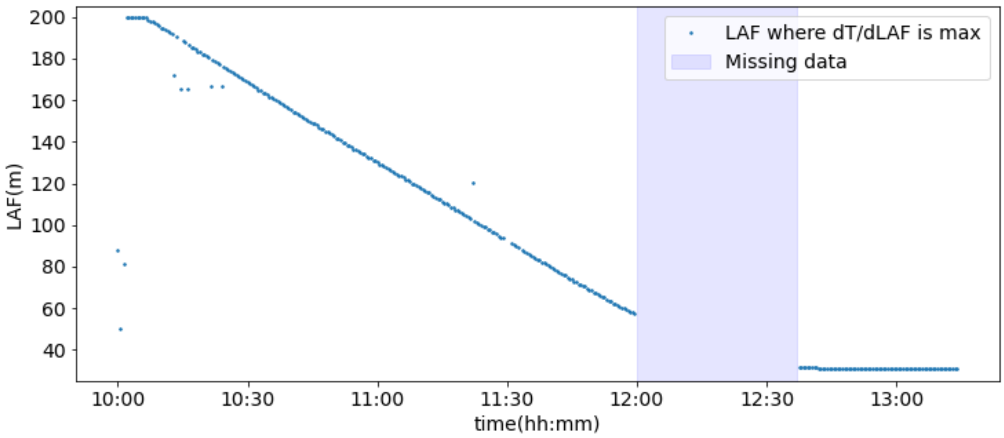

Figure 5.2: The length along fiber (LAF) coordinate where the gradient is strongest, averaged over a period of 30 seconds. Some data is missing as a result of the DTS machine malfunctioning, as indicated by the shaded purple area.

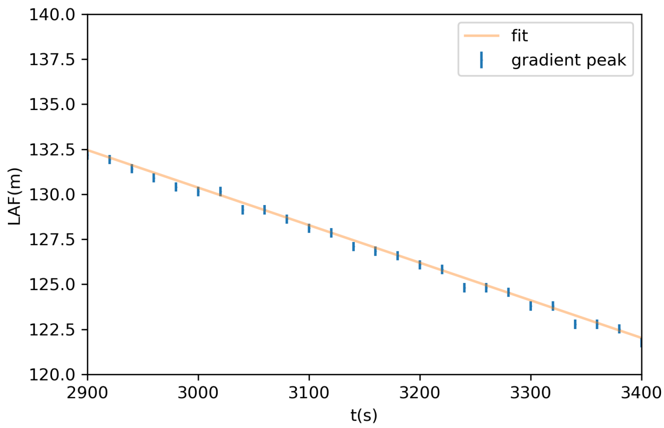

Figure 5.3: The distance from the data points to the actual gradient maximum varies slightly with each measurement. This gives a measure for the measurement uncertainty. This plot is a zoomed in version of Figure 5.2 in order to visualize the uncertainties more accurately.

Taking the distances to the fitted linear trend gives the uncertainty for each data point. This method yields an average uncertainty of 0.26m along the LAF coordinate. This result agrees with the manufacturer's specifications of having a 0.25m resolution. The result is significant as it proves that we can not only measure every 25cm, but also localize gradients at this length scale.

By the known helical slope of the coil, the LAF coordinate directly translates to an accuracy in the z-direction. With the geometrical parameters set for the coil, an uncertainty of 1.25 mm is found for this particular method of localizing gradient maxima. The measurement resolution and accuracy are very high in comparison to traditional temperature sensor resolutions. generally, measurement resolutions are on the order of 0.1 to 1 m.

5.1.2. Horizontal localization

The possibility of extracting information in the horizontal plane was also briefly investigated. To this end, the coil was horizontally submerged in icewater in a similar fashion to the vertical experiment, where the level rises slowly to the top. The results of this experiment are shown in Figure 5.5 and Figure 5.6. From the start of submersion there is a clear spread in points, which corresponds to the fiber moving between cold and warm sections.

One interesting artifact is that the spread does not cover the full range between the air and water temperature, but rather varies between an intermittent temperature. This can be attributed to the effect of thermal conduction within the cable, along with the fact that the DTS is an integrating measurement method. That is to say that the Gaussian spread of measurements extend beyond the neighbouring points at a 0.25m distance. These factors have a 'damping' effect on the measurement, resulting in less significant fluctuation. Therefore, temperature fluctuation amplitudes will not exactly match the actual temperature gradient imposed on the two hemispheres of the coil, but will rather vary between intermittent values.

Another notable observation is the aliasing effect in the measurements. Figure 5.6 shows a temperature oscillation approximately every meter, which corresponds to the expected winding length for our coil diameter of 0.32m. However, in Figure 5.5 another oscillation is seemingly at a much lower spatial frequency. Note that the points in the latter plot are not connected for clarity. The perceived lower frequency oscillation is due to a discrepancy between the winding length and amount of measurement points within it. Theoretically, there should be exactly 4 measurements per revolution, while in reality this will vary slightly. This results in the perceived effect of oscillation, as measurement points will shift with respect to the previous oscillation.

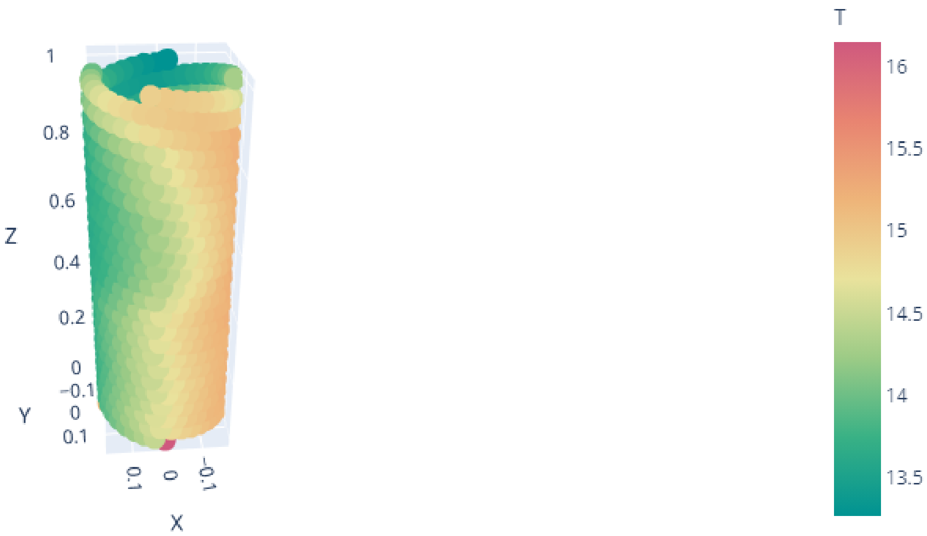

Figure 5.4: 3D plot of the horizontal ice experiment at a certain timestep. It is clearly possible to discern some variance in the horizontal direction, as is demonstrated by the distinct waterline on the coil. However, DTS accuracy and design tolerances result in a line along the length of the coil that is not exactly straight

From this experiment we can conclude that variations in the horizontal plane can be discerned, as is further demonstrated in Figure 5.4. However, for now the resolution is deemed not high enough to perceive temperature gradients with sufficient accuracy along this axis.

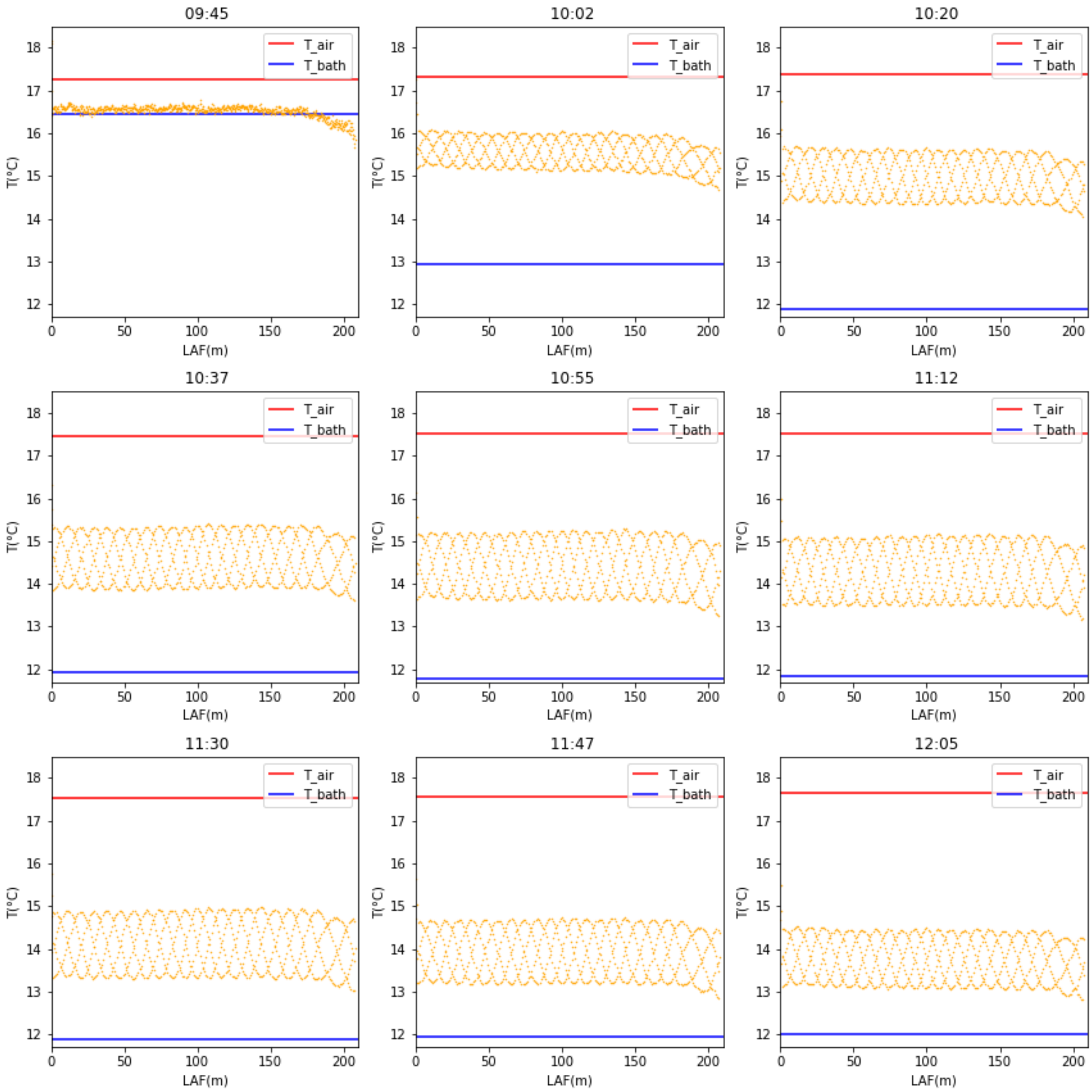

Figure 5.5: The coil is slowly submerged in rising ice water in a horizontal tank. As the cold water hits one hemisphere of the coil, we observe a spatial fluctuation between hot and cold temperatures at the winding frequency of the coil, as expected. Note that as the cold water level rises, the average of the fluctuating signal moves towards the temperature of the cold water as the amplitude stays approximately constant. The temperature does not fluctuate between the air temperature and cold bath temperatures, but rather has a lower amplitude. This is due to thermal conduction in the cable and the correlation of adjacent measurement points. At a circumference of 1 meter, there are only 4 measurement points per rotation.

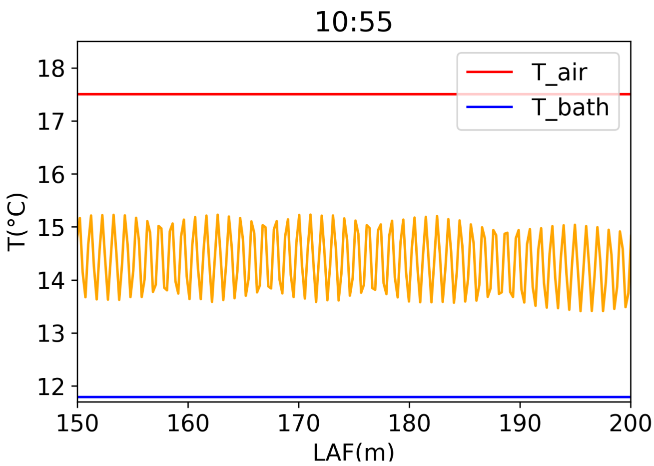

Figure 5.6: Zoomed in plot of the horizontal submersion experiment at 10:55. This plot depicts a higher spatial frequency than the apparent one in Figure 5.5. Clearly, the temperature oscillates at the winding frequency, as expected. The oscillation follows an envelope, which causes the apparent fluctuation in Figure 5.5. This lower frequency oscillation can be attributed to the circumference of the coil not being *exactly* equal to 1 meter, which causes a shift in positions along the coil.

5.1.3. Precipitation: evaporative effects

When the coil becomes wet, for example as a result of precipitation, there arise notable artifacts in the temperature profiles, as shown in Figure 5.7. These effects can be attributed to evaporative cooling of the setup. The reason for the artifacts is the storage of water on the support rings of the coil. As the suspended fiber dries out, the rings are still being cooled as a result of evaporation due to their larger capacity to hold water droplets. As a result, cold spikes can be seen along the profile.
These artifacts often make up a relatively small part of the data, and can therefore be filtered out to yield a usable dataset, even in moist conditions. It is however important to take these effects into account. The artifacts will generally appear for several hours after wetting the coil, depending on external factors such as temperature, radiation and wind.

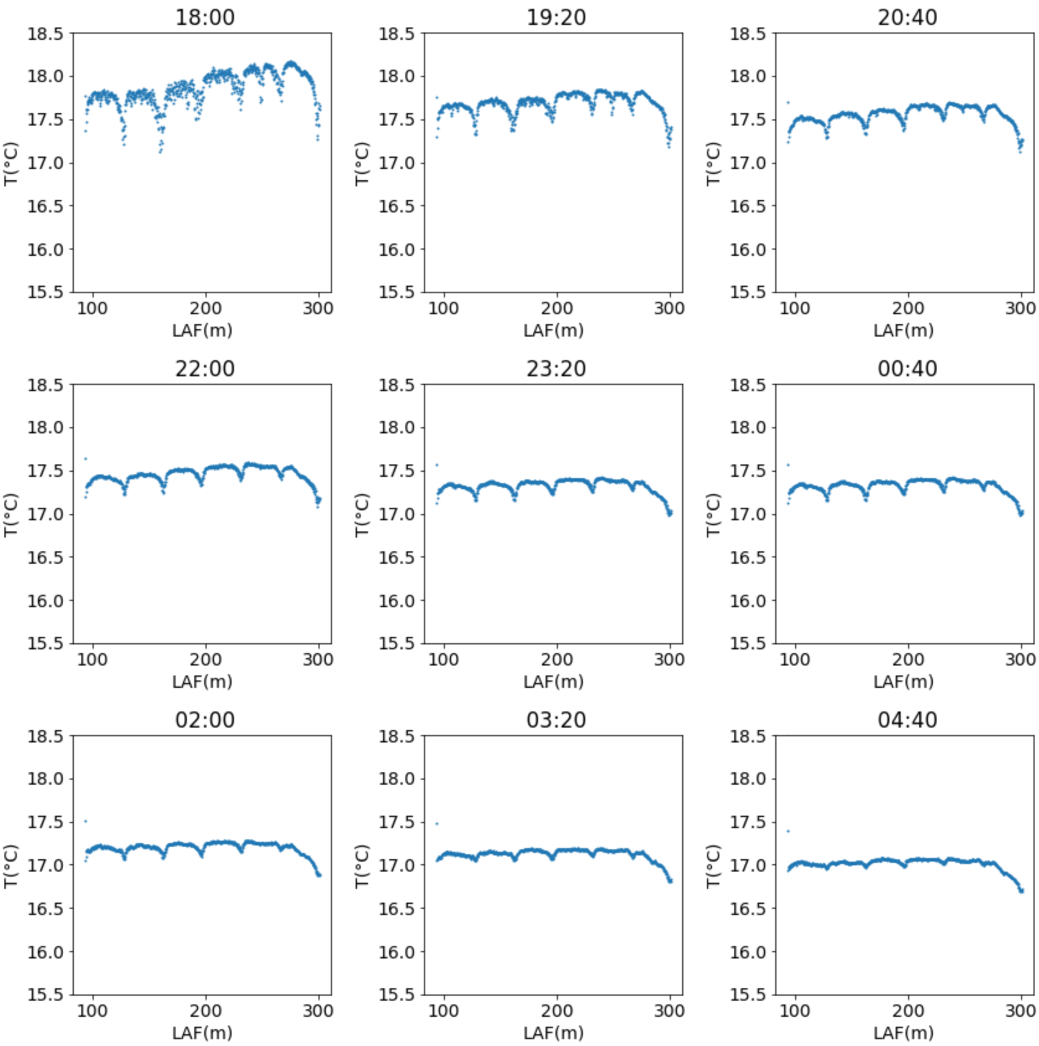

Figure 5.7: The effects of evaporation on the coil. The coil was fully submerged and left to dry overnight in the lab. The figure shows the artifacts becoming less significant over time upon drying up.

5.1.4. Effects of wind: forced convection

Using a hair dryer, warm air was blown through the coil to examine permeability. The results of this experiment are shown in Figure 5.8. A clear spike can be identified where the hot air hits the coil. There is evidently a spread in temperatures, forming a band between low and high temperatures, which is most significant at the position of the heater. The spread is caused by the temperature difference between the front and back of the coil, as is demonstrated by 5.9. The spatial frequency of the temperature variation is exactly equal to the winding frequency. The magnitude of the spread is caused by several factors, such as turbulent mixing of the warm flow with cooler ambient air. However, one impacting factor is also the permeability of air through the coil. Qualitatively, this result shows that a part of the air permeates the front of the coil to heat up the back, as is illustrated by the fact that the temperature band minimum is not at ambient temperature.

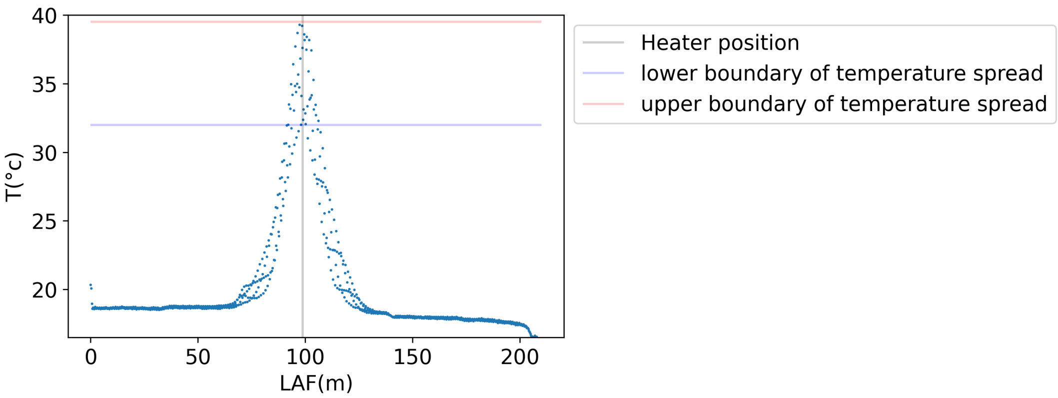

Figure 5.8: A hair dryer was pointed at the center of the coil. The flow of warm air through the coil creates the peak in the center of the figure. A spread in temperatures can be seen at the peak as a result of the temperature gradient across the front and back of the coil, as is further illustrated in Figure 5.9.

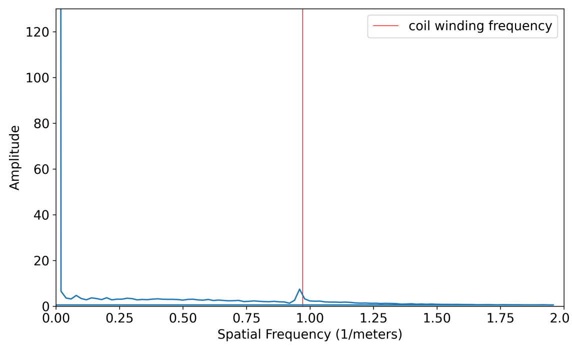

(a) Spectral plot of the temperature within the area where there was no forced convection

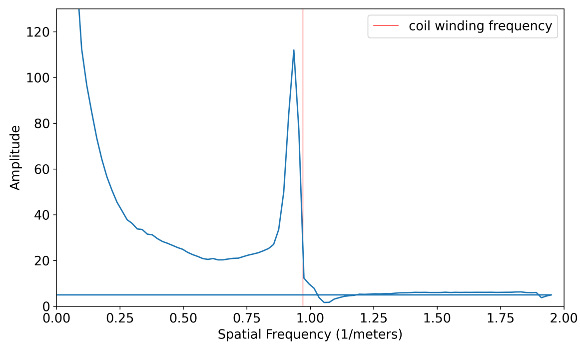

(b) Spectral plot of the temperature within the area where there was forced convection

Figure 5.9: The difference between the case with and without forced convection can be observed from these 2 plots. Note the peak at the winding frequency of the coil. Forced convection imposes a temperature gradient on the coil in the horizontal plane. This gradient causes the temperature fluctuation at the winding frequency.

5.1.5. Long-wave radiation effects

The setup was irradiated by long-wave radiation from a 2kW heat lamp. Half of the setup was shielded from radiation, while the other half was fully exposed. The results are depicted in Figure 5.10. The support rings clearly absorb radiation, heating the frame locally. This results in higher temperature peaks at these points. There is also a clear spread in temperatures in the shape of a band. This artifact is due to the fact that the backmost fiber absorbs less radiation than the sections in front. This manifests itself in the form of a temperature gradient in the x-y plane, much like the horizontal ice bath experiment. This is further supported by Figure 5.11, where a spectral analysis shows a significant peak at the coil winding frequency. This result indicates that the coil absorbs radiation to a degree where horizontal temperature gradients emerge within itself, as a result of shading.

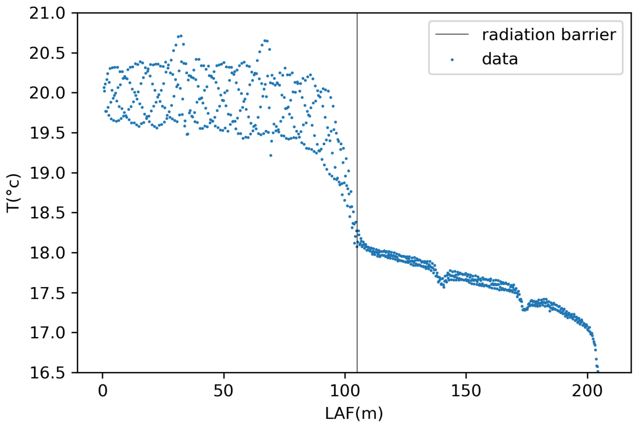

Figure 5.10: The effects of long-wave radiation on the coil. Half of the coil is shaded, while the other half is exposed to the radiation. A temperature gradient between the back and front of the coil is observed, as well as increased absorption at the support ring interfaces.

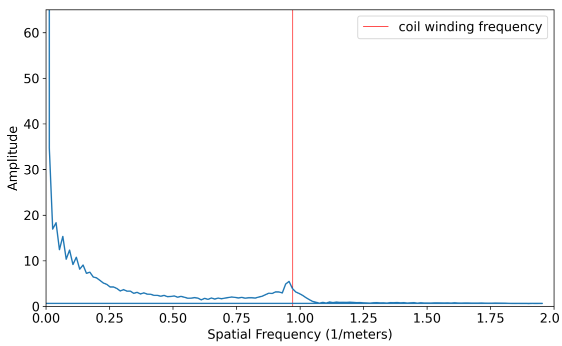

(a) Spectral plot of the temperature within the area where the was coil was shaded

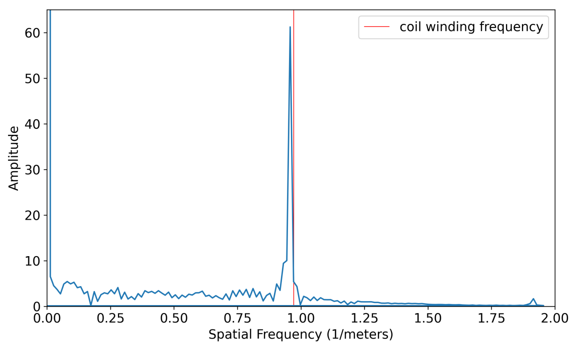

(b) Spectral plot of the temperature within the area where the coil was irradiated

Figure 5.11: Spectral analysis of radiation exposed section vs the shaded section of the coil. A peak is found at the spatial winding frequency of the coil, indicating a horizontal temperature gradient imposed by the radiation.

5.2. Field experiment at Cabauw observatory

Measurements at Cabauw were conducted over a period of approximately one month. There are two distinct surveying periods: the first ranges from 26-03-2024 to 1-4-2024 and the second one from 08-04-2024 to 18-04-2024. During this surveying period, the setup was exposed to a wide range of weather conditions. Several characteristic temperature profiles were identified and presented in the following section. The profiles are validated by the KNMI air temperature measurement at 1.5m height. Other variables from Cabauw measurement stations were included for further analysis. These include: cumulative Precipitation over a 30 minute interval in mm, surface solar radiation balance in $\frac{W}{m^2}$ and windspeed in $\frac{m}{s}$. These parameters can help identify the cause of certain artefacts found in the temperature profiles.

Figure 5.12 depicts a classical stable temperature profile found from the Cabauw field experiment. A 30 minute average was taken to yield the depicted profile. The profile follows the logarithmic profile above the canopy, in accordance to MOST 2.1.1. the profile was recorded in the evening, characterized by a negative radiation balance, resulting in a cool surface. At night, the dense, cold air resides near the ground, resulting in a stably stratified situation. this is characterized by the positive temperature slope with height.

To demonstrate the quality of the dataset, some preliminary analyses were done on this profile. Firstly, the **determination of** θ_* can be done using two different methods. Primarily, the profile can be logarithmically plotted, which according to Equation 2.12 should yield a line with a slope determined by $\frac{\theta_*}{\kappa}$. Transforming the profile accordingly and extracting θ_* yields a value of 0.143 $\pm 0.005K$. The profile can also directly be fitted using a python curve fit routine of the form of Equation 2.12. This yields a similar result of 0.145K. Note that before only 2 or 3 measurements are available for such estimates. Here, a larger number of points can be included, and the validity of the 'log-law' can be assessed at the same time.

Additionally a **Gradient analysis** can be done to quantitatively compare the validity of different physical models. To this end, the profiles are smoothed using a moving average with a window of 50 datapoints. This is to ensure that the gradient can be accurately determined from the data. It is noteworthy that this method introduces loss of data at the edges of the array, as an intrinsic property of the moving average method. the choice for the window size is determined from a trade-off between data loss and data roughness. The gradient can be determined using standard python routines, which results in a gradient depicted in Figure 5.13. Note that, once again, such an analysis is usually not possible with conventional measurements which lack vertical resolution.

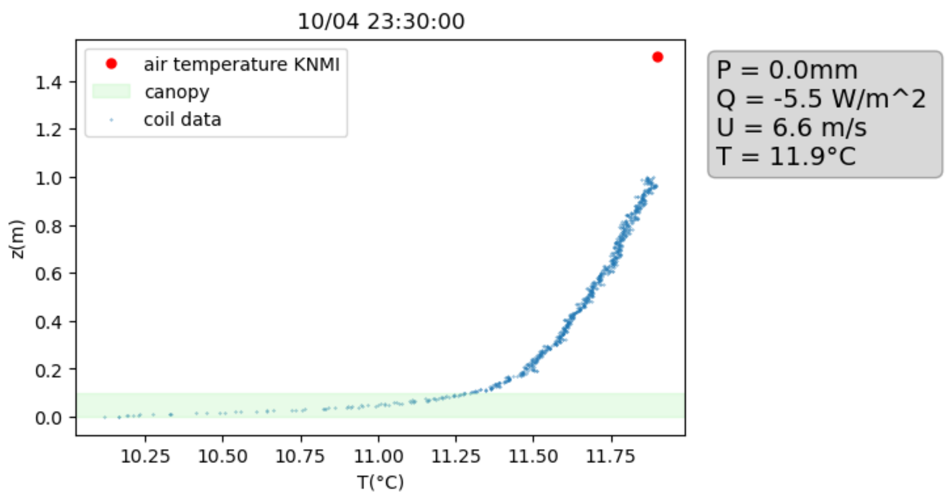

Figure 5.12: A temperature profile, as measured with the coil in stable conditions. Values in the adjacent box correspond to cumulative rainfall over a half hour period, total radiative balance, total windspeed and the air temperature at 1.5m respectively. These values are sourced from other Cabauw field measurements.

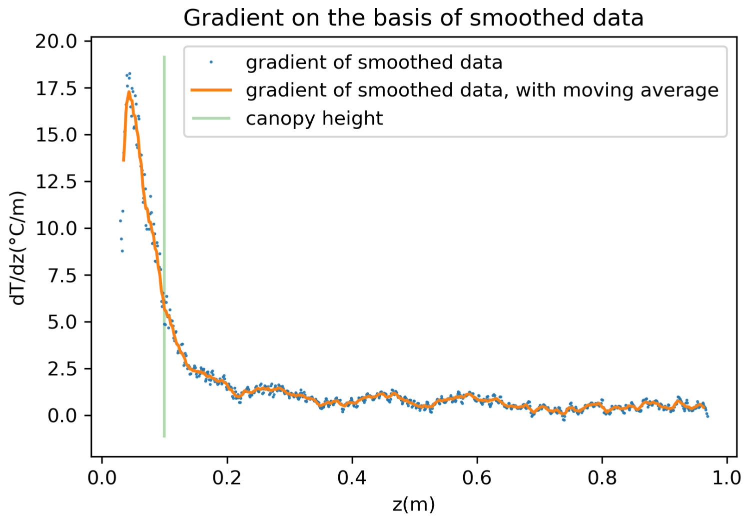

Figure 5.13: Gradient of the temperature profile depicted in Figure 5.12

Another novel possibility that this dataset brings is the potential for **analysing temperature profiles *within* the thin grass layer**. Such information can be used to study internal canopy dynamics. There are approximately 80 data points within the canopy, at a 5 second temporal resolution. Figure 5.14 demonstrates nontrivial behaviour within the canopy, in the form of an inversion of the temperature profile. The resolution of the dataset allows for the determination of in-canopy gradients, which can be insightful for future studies into unifying the classical MOST profiles [3] with other transport mechanisms within the grass, such as canopy diffusion approaches [9].

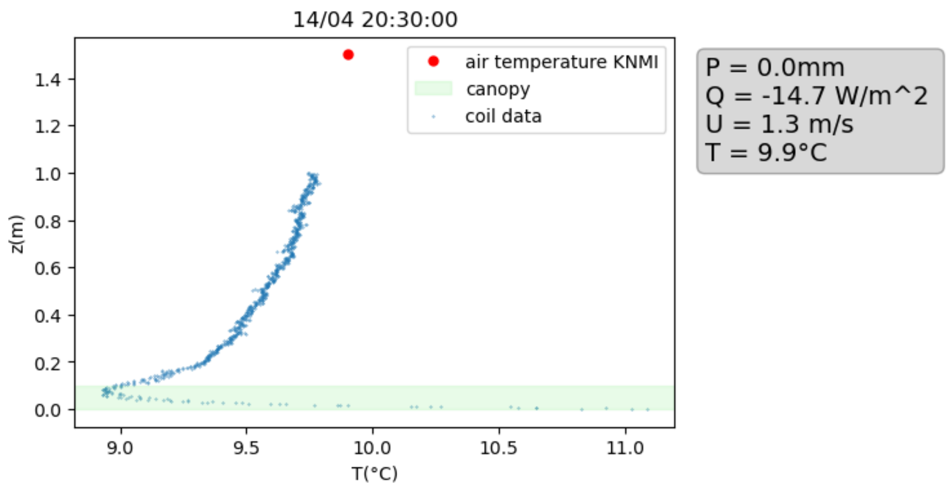

Figure 5.14: Another temperature profile in stable conditions is depicted. Moreover, there is a profile inversion visible within the canopy, which has a temperature minimum within the canopy.

In accordance to the results of the lab tests, some artifacts were found in the data as a result of sub-optimal weather conditions, such as rain. Additionally, instrument limitations yielded some artifacts, such as high radiation absorption during the day. Figure 5.15 shows cooling artifacts as the support ring interfaces as a result of evaporation after rainfall. This corresponds well to results found before in Figure 5.7. As previously mentioned, these profiles can still be filtered to exclude the ring effects to yield a useful dataset as a result of redundancy in the spatial measurement resolution.
Finally, a profile is shown in Figure 5.16 with very high solar radiation absorption. Some previously identified artefacts can be seen, such as the temperature gradient in the horizontal plane, caused by partial shading of the coil. This results in a wider spread of temperatures, as previously demonstrated

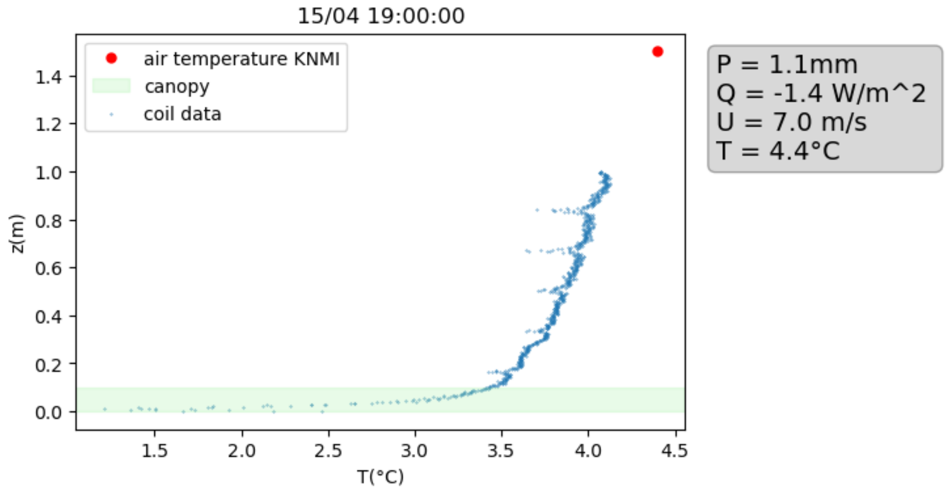

Figure 5.15: The effects of precipitation, and subsequent evaporative cooling is clearly demonstrated by the appearance of cooling artifacts at the support rings, as was previously demonstrated in the lab in the lab experiments.

in Figure 5.10. Additionally, some influence of the support rings can be seen again. Some artifacts are newly observed, such as the one at the top of the coil. There seems to be a slant towards cooler temperatures at the top of the coil. This could be explained by radiation hitting the coil at an angle. This effect will further be discussed in section 6.2.
Furthermore, the Cabauw air temperature measurement shows a discrepancy between the profile and the measured air temperature in the field, which is beyond reasonable error margins, taking into account measurement uncertainty and location. This likely demonstrates a shift in the temperature profile as a result of fiber heating due to radiation absorption.

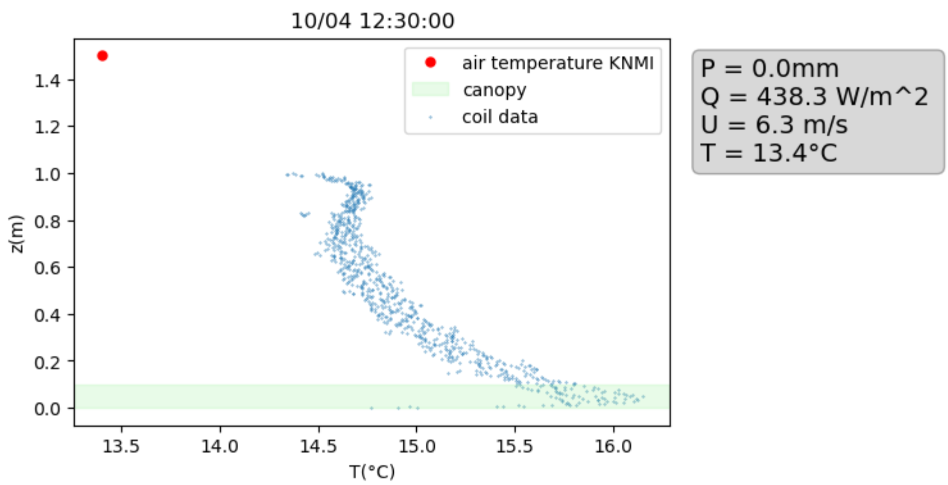

Figure 5.16: The effects of high radiation absorption become apparent. A spread in measurements appears in a similar fashion to the lab experiments, as a result of partial shading effects that impose a horizontal temperature gradient on the coil. An additional artifact is observed at the top of the coil, which has not been observed before. This effect is likely due to radiation hitting the coil at an angle. For further analysis, see section 6.2.

5.2.1. Auxiliary measurements

The 5m mast and soil screw were included at Cabauw to further expand the measurement domain and to validate the results from the coil. An example of the continuity between the coil and the soil screw is given in Figure 5.17.

Another example is given in Figure 5.18, where the mast data is also included. In this case the profiles agree well with respect to each other. A very large gradient is noticeable at the soil-canopy interface. This could be due to a strongly insulating 'mulch' layer, comprised of decomposed organic material overlying the soil.

Profiles are not always in agreement, as can be seen in Figure 5.19, where both the absolute profile and the gradient between the mast and coil do not correspond.

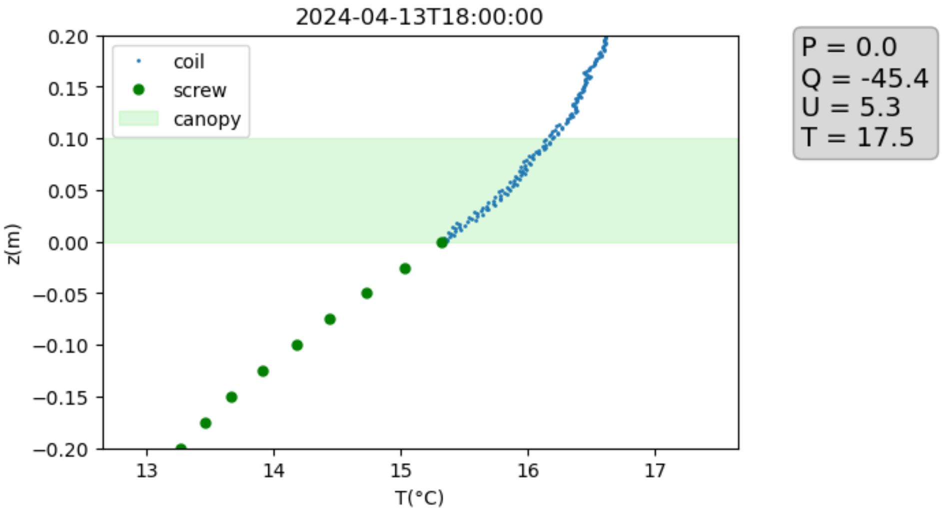

Figure 5.17: A close up of the soil-canopy-air interface, demonstrating the continuity of the coil and soil screw measurements at some instances

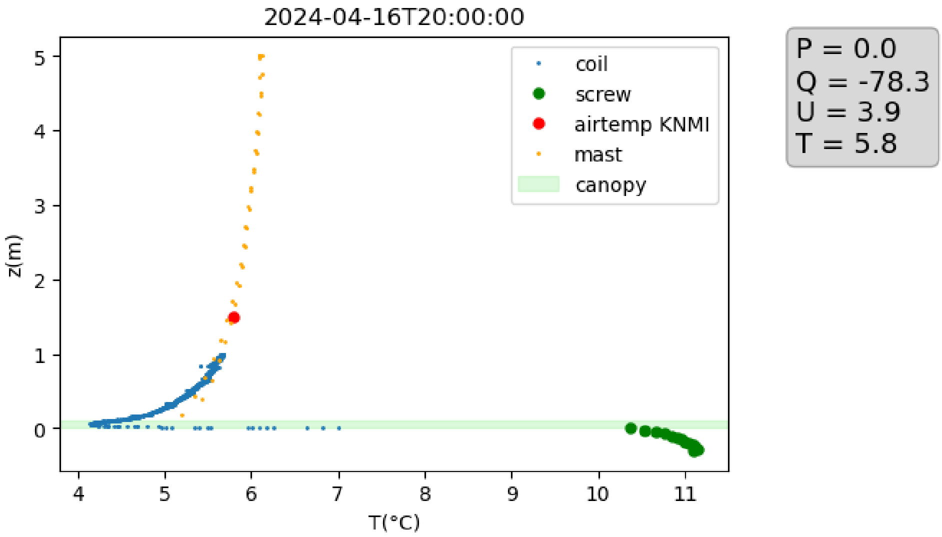

Figure 5.18: An overview of all measurements at a certain timestep where all profiles agree well. A very large temperature gradient is noticeable near the surface.

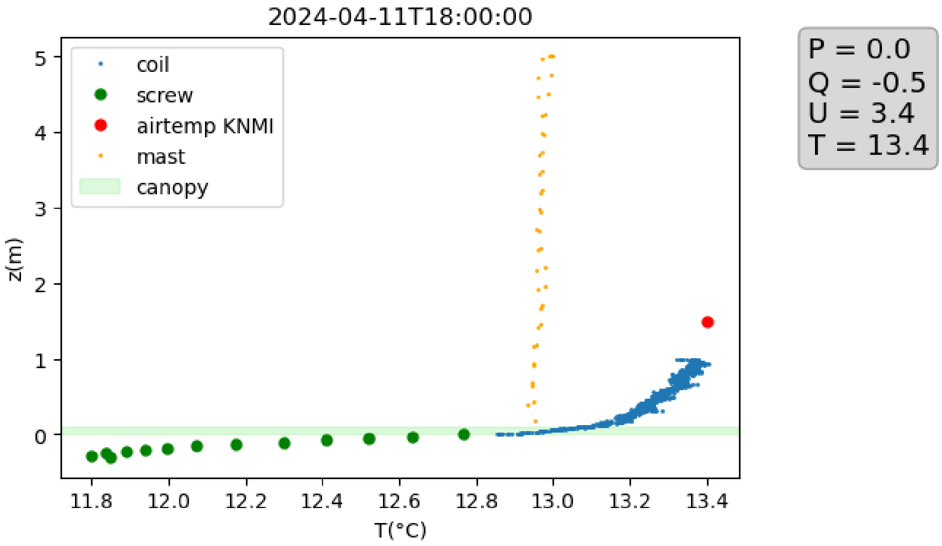

Figure 5.19: Profiles do not always agree well and may sometimes be shifted with respect to one another. Gradients may also be discontinuous, as demonstrated by the discrepancy between the coil and mast profiles.

6
Discussion

6.1. Setup and design iteration

There are several design aspects that are yet to be improved for future campaigns. Another iteration in the design cycle would have further improved on the setup. However, due to time constraints, the functional product was directly taken into the field as it had passed all essential criteria in the lab tests at that time. Some recommendations for future improvement are given below.

In the initial design stage, the decision was made to omit the bottom support ring, as that section of the coil would already be supported by the multitude of ground stakes that anchor the coil to the ground. However, the tensile stress on the coil, due to the winding of the fiber, turned out to be much more significant than initially expected. This resulted in the use of a wooden auxiliary ring which slotted over the ribs to support the coil during the winding process. Removing this ring after installation compromises the structural integrity of the coil as a result of the stress on the frame. It is therefore recommended to include the bottom support ring on the coil.

Furthermore, some revision on the fiber clamping mechanism is in order. The current design uses Lester screw terminals with rubber dampers to fasten the fibers. They provide very good grip on the fiber, however, the screws have an effect on the integrity of the cable. Significant signal loss was detected on one of the two Lester terminals. Signal losses can be compensated by using a double ended configuration on the DTS. Nonetheless, it is advantageous to limit signal loss to a minimum to keep the signal to noise ratio as high as possible. To this end, it is recommended that the Lester terminals are fitted with more resilient dampers and that they are not over-tightened. Other means of fastening the fiber can also be investigated, keeping in mind the need for relatively high clamping force to keep the fiber at the required tension.

Winding the coil inflicts a torque on the coil. With each revolution, the fiber pulls the frame in the direction of winding. This can cause the frame to experience torsional shift over the full length of the coil. It is important to be mindful of this when winding the coil, as these effects can be compensated by properly supporting the ribs while winding. Torsion within the frame does not impact the measurements. However, it may impact the structural integrity of the frame when it is excessively present.

Finally, a significant source of uncertainty in the field campaign is the determination and monitoring of grass height. The grass height was measured every time that the site was visited. This was done by estimating the mean grass height using a measuring tape. Future campaigns would greatly benefit from an improved method of accurately characterising the grass around the measurement location. The measurements would ideally be more spatially accurate and more frequent in time.

6.2. Field experiment artifacts

There are some notable artifacts that emerge from the field data, some of which were already identified in the lab calibration experiment.

For instance, the **support ring artifacts** emerge after precipitation or during periods of high solar irradiation. Both are observed in the lab results and Cabauw field experiment. These artifacts can be circumvented by omitting them from the data. The loss of information is limited, as the artifacts often only compose a small section on the data. Additionally, the rings are evenly interspaced along the vertical coordinate, allowing for interpolation between the omitted sections. These artefacts therefore do not pose any problem for the overwhelming majority of profiles.

A more significant effect is attributed to **radiation bias** in the measurements. As is observed in Figure 5.16 there is a discrepancy between the measured air temperature at Cabauw and the projected extrapolation of the coil profile. This is due to a large radiation bias, as absorption is high at this time. The frame and fiber absorb significant amounts of radiation, increasing the measured temperature with respect to the ambient air temperature. Consequently, there will be exceptional cases where temperature is significantly biased as a result of high solar radiation absorption. The effect of radiation on glass fiber cables has been studied in the context of DTS and can be, to a certain degree, corrected for [25] [26]. This requires special attention to the absorbed radiation when processing data.

Another potential source of bias in the data is wetting of the DTS fiber. As mentioned before, ring artifacts will become prevalent after a precipitation event. Additionally, as with radiation, there will be an overall cooling bias over the whole length of the fiber as a result of it being wet. When the fiber is wet, it will attain a 'wet bulb temperature' as a result of evaporative cooling. This effect has been thoroughly studied and is even implemented as a measurement technique to measure wind speeds [27] [28].

Another artifact of the coil that was not observed in the lab experiment is **a deviation at the top of the coil**. Temperature profiles seem have a tendency to cool down towards the top section of the coil. One possible explanation is attributed to differential heating as a result of high solar radiation. These artifacts are most significantly present during periods of high absorption of solar radiation, as can be seen in Figure 5.16. Analysing this plot, we notice a similar band-like spread in temperature measurements in the lower part of the coil, as we would expect from the lab experiments shown in Figure 5.10. Additionally, we observe the effect of the support rings along consistent intervals as relatively cool peaks. Towards the top of the coil, the temperature spread tends to get more narrow. This narrowing can possibly be attributed to the fact that both the front and back ends of the coil are irradiated in this section, as the back part of the coil is not shaded by the front. This in turn results in a lower temperature difference between the front and back part of the coil, which will shift the profile to the warm irradiated regime. The perceived slant towards cooler temperatures at the top can be attributed to the effect of the support rings. When following the pattern of lower support rings towards the top, it becomes apparent that they follow a consistent pattern, to which the top ring is no exception. The coil is merely perceived to cool towards the top, due to the contrast between the two aforementioned phenomena of band-narrowing and support ring cooling.

7
Conclusion and recommendations

The central challenge in this thesis was to design a measurement setup that can measure temperature profiles through grass at a high resolution. The aim was to probe temperatures on the millimeter scale, which creates the potential to study the large gradients near the surface. Additionally, we would like to study temperature profiles within the canopy. Reaching both of these objectives was previously impossible, as a result of measurements lacking in vertical resolution and accuracy.
The preliminary analysis on the data demonstrates a conclusive success of the field experiment. Gradients can be examined down to the canopy with sufficient accuracy to quantitatively compare models that describe temperature profiles near the canopy top. Additionally, there are approximately 80 datapoints within the canopy at a 5 second resolution, which adds the opportunity for studying temperature profiles within the canopy.
We can therefore conclude that we have indeed reached our goal of developing and implementing a method that measures temperature profiles at a high resolution. The method yields temperature profiles through the canopy at a 1.25mm resolution, with a temperature precision of 0.1K.

7.1. Applications and future research

One branch of ongoing research studies the temperatures near the canopy top, with the aim of arriving at a physically consistent alternative model to MOST. Multiple proposals for such an adaptation have been done. It was previously challenging to verify them in a conclusive and quantifiable manner. The data from the field experiment yields the possibility to overcome this issue and can be used to quantitatively describe temperatures close to the canopy top in such a way that the validity of several models can be compared.
A more in-depth study into the comparison of these models should also take into account stability corrections. These corrections are significant in this case and should not be omitted in further analysis [3] It is recommended to perform similar in-depth analysis on gradients near the canopy as in previous field experiments [8]. This can potentially lead to new and better models to model atmospheric temperature above canopies, as well as improve physical understanding.

Furthermore, θ_* can be determined from the measurements. From the data, θ_* was determined to be 0.143K in the case of the stable profile given in Figure 5.12. It was determined to an accuracy of 0.005 K. Accurate estimation of this parameter is possible as a result of the high spatial resolution of the temperature profile.

Finally, models for transport dynamics within the canopy, such as the diffusive canopy model [9], can be validated in the future using the data. These results will prove essential in the further development of such models, and will help shape them in a more physically consistent manner.
The goal of future theoretical development should be to unify the in-canopy and above canopy heat exchange descriptions. Such a theory would predict temperature profiles in a continuous way from the soil, through the canopy top, up into the atmosphere. These models can both be validated and inspired by the observations done in this campaign. For example properly modeling the non-trivial inversion that

was seen in Figure 5.14, in contrast to the much used linear ’skin-resistance’ model.

7.2. Experimental setup

As illustrated in the previous section, the experimental setup yielded results that were very encouraging. However, there remain several aspects that leave room for improvement.

Firstly, signal loss due to overtightened Lester terminals should be prevented in future use of this method. It is recommended that they be merely moderately fastened, as that will already supply sufficient tension for keeping the fiber in place. Any future improvements on the design could include alternative fastening method, provided they meet the criterion for proper cable tension.

Moreover, the coil used at Cabauw was purposely designed without its bottom support ring, as the soil was assumed to provide enough rigidity. Retrospectively, this ring should not have been omitted for structural reasons. The cable winding process is next to impossible without the structural support of a bottom ring. Additionally, removing any temporary placeholder for a support ring in the field is impossible, due to excessive strain on the frame as a result of the high cable tension. It is therefore recommended to include the bottom support ring in any case.

Another important aspect relates to the design of the 5m mast. The cable was observed to periodically lose tension as a result of insufficient clamping strength at the start and end of the mast. Over time, this may result in a coordinate shift for the temperature data. To prevent this, it is advised to revise the clamping method. Lester terminals could possibly pose a solution, provided that they are not overtightened. A similar stencil to the coil could be laser cut to firmly hold the terminal in place.

Finally, it is recommended to research more rigorous ways of determining canopy height. The most significant uncertainty of the field experiment resides in an accurate description of grass height. In this instance, nominal grass height was determined by taking the approximate mean height of grass blades in a plot close to the coil. A more rigorous measure for this characteristic could greatly improve accuracy of the characteristic length scales.

Acknowledgements

The completion of my thesis would not have been possible without the help of some people, to whom I would like to extend my sincere gratitude.

From the FruitFrost team, I would like to thank Bas van de Wiel and Marie-Claire ten Veldhuis for their continuous guidance and support throughout this project. I could not have wished for a better, more motivating supervisor than Bas. Furthermore I would like to thank the team of PhD candidates: Yi Dai and Judith Boekee for their help and support, with special gratitude to Gijs Vis for taking the time to be my secondary supervisor. I would also like to thank my fellow grad student, Sabine van Dijk, for her help and support both in the field and with writing my thesis.
I would like to thank Wim Bouwman for taking the time to be part of my examination committee.

Furthermore, my gratitude goes out to KNMI staff members Mariska de Koning and Guido van Wegen for their assistance in the Cabauw field campaign, without whom, the experiment would not have been possible.

Building my designs took several long days of manufacturing in the Applied Physics makerspace. Here, I was accompanied by three long time colleagues: Ron Breider, Tom Haanstra and Diederik la Haye. I would like to thank these 'Maketiers' for allowing me to use their workspace and tools for my thesis project and for all the expertise and great stories they have shared with me over the years.

Finally, I would like to thank my secondary instructor: Rolf Hut. Both for the guidance during this project, but especially for four years of working together on teaching the 'DEF' course and for the many things it has taught me. I look back on it with great pleasure.

References

[1] W. L. Physick and J. R. Garratt. “Incorporation of a high-roughness lower boundary into a mesoscale model for studies of dry deposition over complex terrain”. In: *Boundary-Layer Meteorology* 74.1–2 (Apr. 1995), pp. 55–71. DOI: `10.1007/bf00715710`.

[2] A. A. Holtslag et al. “Stable atmospheric boundary layers and diurnal cycles: Challenges for weather and climate models”. In: *Bulletin of the American Meteorological Society* 94.11 (Nov. 2013), pp. 1691–1706. DOI: `10.1175/bams-d-11-00187.1`.

[3] A. F. Moene and J. C. van Dam. *Transport in the atmosphere-vegetation-soil continuum*. Cambridge University Press, 2014.

[4] G. B. Bonan et al. “Modeling canopy-induced turbulence in the Earth system: A unified parameterization of turbulent exchange within plant canopies and the roughness sublayer (CLM-ml v0)”. In: *Geoscientific Model Development* 11.4 (Apr. 2018), pp. 1467–1496. DOI: `10.5194/gmd-11-1467-2018`.

[5] R. Meier et al. “Impacts of a revised surface roughness parameterization in the community land model 5.1”. In: *Geoscientific Model Development* 15.6 (Mar. 2022), pp. 2365–2393. DOI: `10.5194/gmd-15-2365-2022`.

[6] J. Sun. “Diurnal variations of thermal roughness height over a grassland”. In: *Boundary-Layer Meteorology* 92.3 (Sept. 1999), pp. 407–427. DOI: `10.1023/a:1002071421362`.

[7] P. G. Duynkerke. “The roughness length for heat and other vegetation parameters for a surface of short grass”. In: *Journal of Applied Meteorology* 31.6 (June 1992), pp. 579–586. DOI: 10.1175/1520-0450(1992)031\<0579:trlfha\>2.0.co;2.

[8] J. Boekee et al. “Improved description of temperature profiles over short vegetation: rethinking the roughness height”. In: *Boundary layer meteorology* (2024). Approved for publication.

[9] B. J. H. van de Wiel et al. In: *Heat transfer through grass: A diffusive approach* (Mar. 2022). DOI: `10.5194/egusphere-egu22-8030`.

[10] M. Sonneveld. *Analysis of the soil-air energy balance*. Thesis report (TU Delft). 2023.

[11] M.L. Zeller et al. “The NY-Ålesund TurbulencE Fiber Optic eXperiment (NYTEFOX): Investigating the Arctic boundary layer, Svalbard”. In: *Earth System Science Data* 13 (7 2021). ISSN: 18663516. DOI: `10.5194/essd-13-3439-2021`.

[12] N. Nowak. “Remote Sensing of the Lower Atmosphere: From Surface Concentration to Mixing Layer Height”. PhD thesis. Feb. 2022. DOI: `10.13140/RG.2.2.30055.93605`.

[13] J. R. Garratt. “Extreme maximum land surface temperatures”. In: *Journal of Applied Meteorology* 31.9 (Sept. 1992), pp. 1096–1105. DOI: 10.1175/1520-0450(1992)031\<1096:emlst\>2.0.co;2.

[14] J. Wiernga. “Representative roughness parameters for homogeneous terrain”. In: *Boundary-Layer Meteorology* 63.4 (Mar. 1993), pp. 323–363. DOI: `10.1007/bf00705357`.

[15] E. Florens, O. Eiff, and F. Moulin. “Defining the roughness sublayer and its turbulence statistics”. In: *Experiments in Fluids* 54 (4 2013). ISSN: 07234864. DOI: `10.1007/s00348-013-1500-z`.

[16] T. Foken. *50 years of the Monin-Obukhov similarity theory*. 2006. DOI: `10.1007/s10546-006-9048-6`.

[17] T. Foken et al. “Some aspects of the energy balance closure problem”. In: *Atmos. Chem. Phys.* (Apr. 2006). DOI: `10.5194/acpd-6-3381-2006`.

[18] P. Nollen. *The thermal roughness length: study on a mysterious concept*. Thesis report (TU Delft). 2022.

[19] J. M. Donda et al. “Collapse of turbulence in stably stratified channel flow: A transient phenomenon”. In: *Quarterly Journal of the Royal Meteorological Society* 141.691 (Mar. 2015), pp. 2137–2147. DOI: 10.1002/qj.2511.

[20] J. M. Donda et al. “The maximum sustainable heat flux in stably stratified channel flows”. In: *Quarterly Journal of the Royal Meteorological Society* 142.695 (Nov. 2015), pp. 781–792. DOI: 10.1002/qj.2680.

[21] E.R. Van Driest. “On Turbulent Flow Near a Wall”. In: *Journal of the Aeronautical Sciences* 23 (11 1956). DOI: 10.2514/8.3713.

[22] A. Orlando et al. “A comprehensive review on Raman spectroscopy applications”. In: *Chemosensors* 9.9 (Sept. 2021), p. 262. DOI: 10.3390/chemosensors9090262.

[23] B. des Tombe, B. Schilperoort, and M. Bakker. “Estimation of temperature and associated uncertainty from fiber-optic Raman-spectrum distributed temperature sensing”. In: *Sensors* 20.8 (Apr. 2020), p. 2235. DOI: 10.3390/s20082235.

[24] N. van de Giesen et al. “Double-ended calibration of fiber-optic Raman spectra distributed temperature sensing data”. In: *Sensors* 12.5 (Apr. 2012), pp. 5471–5485. DOI: 10.3390/s120505471.

[25] S. A. de Jong, J. D. Slingerland, and N. C. van de Giesen. “Fiber optic distributed temperature sensing for the determination of Air Temperature”. In: *Atmospheric Measurement Techniques* 8.1 (Jan. 2015), pp. 335–339. DOI: 10.5194/amt-8-335-2015.

[26] B. Schilperoort. “Heat Exchange in a Conifer Canopy: A Deep Look using Fiber Optic Sensors”. English. Dissertation (TU Delft). Delft University of Technology, 2022. DOI: 10.4233/uuid:6d18abba-a418-4870-ab19-c195364b654b.

[27] B. Schilperoort et al. “Technical note: Using distributed temperature sensing for Bowen ratio evaporation measurements”. In: *Hydrology and Earth System Sciences* 22.1 (Jan. 2018), pp. 819–830. DOI: 10.5194/hess-22-819-2018.

[28] J. G. Izett et al. “Missed fog?” In: *Boundary-Layer Meteorology* 173.2 (July 2019), pp. 289–309. DOI: 10.1007/s10546-019-00462-3.

[29] KNMI. *Normale waarden temperatuur – langjarig gemiddelde 1991-2020*. 2020. URL: https://www.knmi.nl/nederland-nu/weer/waarschuwingen-en-verwachtingen/normalentabel.

[30] KNMI. *Storm Ciara*. 2023. URL: https://www.knmi.nl/over-het-knmi/nieuws/storm-ciaran.

[31] Weerstation Westland - De Poel. *Zonnestraling*. 2024. URL: https://www.westland-depoel.nl/vantagevue/ws/wxsolardetail.php.

[32] Weerstation Westland - De Poel. *Rain Detail*. 2024. URL: https://www.westland-depoel.nl/vantagevue/ws/wxraindetail.php.

[33] B. Schilperoort et al. “A distributed-temperature-sensing-based soil temperature profiler”. In: *Geoscientific Instrumentation, Methods and Data Systems* 13.1 (Apr. 2024), pp. 85–95. DOI: 10.5194/gi-13-85-2024.

[34] *Granta EduPack Material Library*. Software. Ansys, Canonsburg, Pennsylvania, U.S. 2023, R2.

[35] Robert McNeel & Associates. *Rhinoceros and Grasshopper*. Version 7, accessed: 2024-05-17. 2024. URL: https://www.rhino3d.com/.

[36] A. Apituley. *Ruisdael Observatory: Cabauw*. Accessed: 2024-06-21. 2024. URL: https://ruisdael-observatory.nl/cabauw/.

[37] C. Kohlmann. *Ruisdael Observatory: Campaigns*. Accessed: 2024-06-21. Aug. 2022. URL: https://ruisdael-observatory.nl/category/campaigns/.

A

Laser cutting files

Beow, the files that generate laser cutting templates for the coil are hosted. These files can be used to generate a custom coil for a wie range of applications:
https://data.4tu.nl/private_datasets/YwuzuOlGmxfit_ek7zUXJ573UB1NQ-3osdINa7TKMUg

Figure A.1 shows the list of parameters that can be adjusted to customize it.

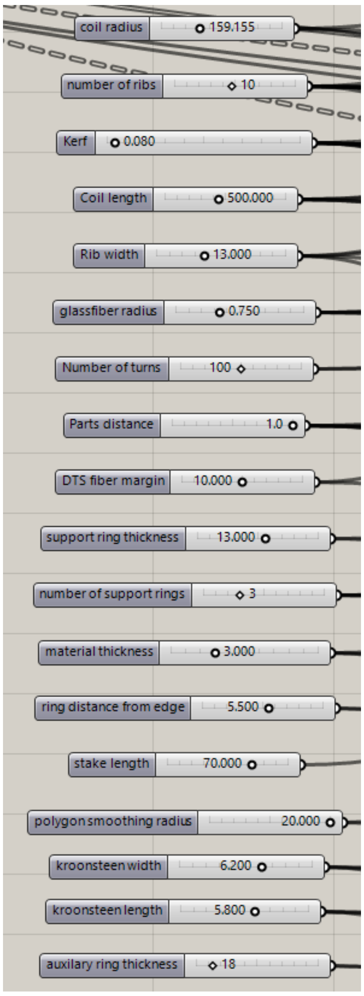

Figure A.1: Adjustable parameters in the svg generator

Figure A.2 shows what the final template used for the Cabauw campaign looks like.

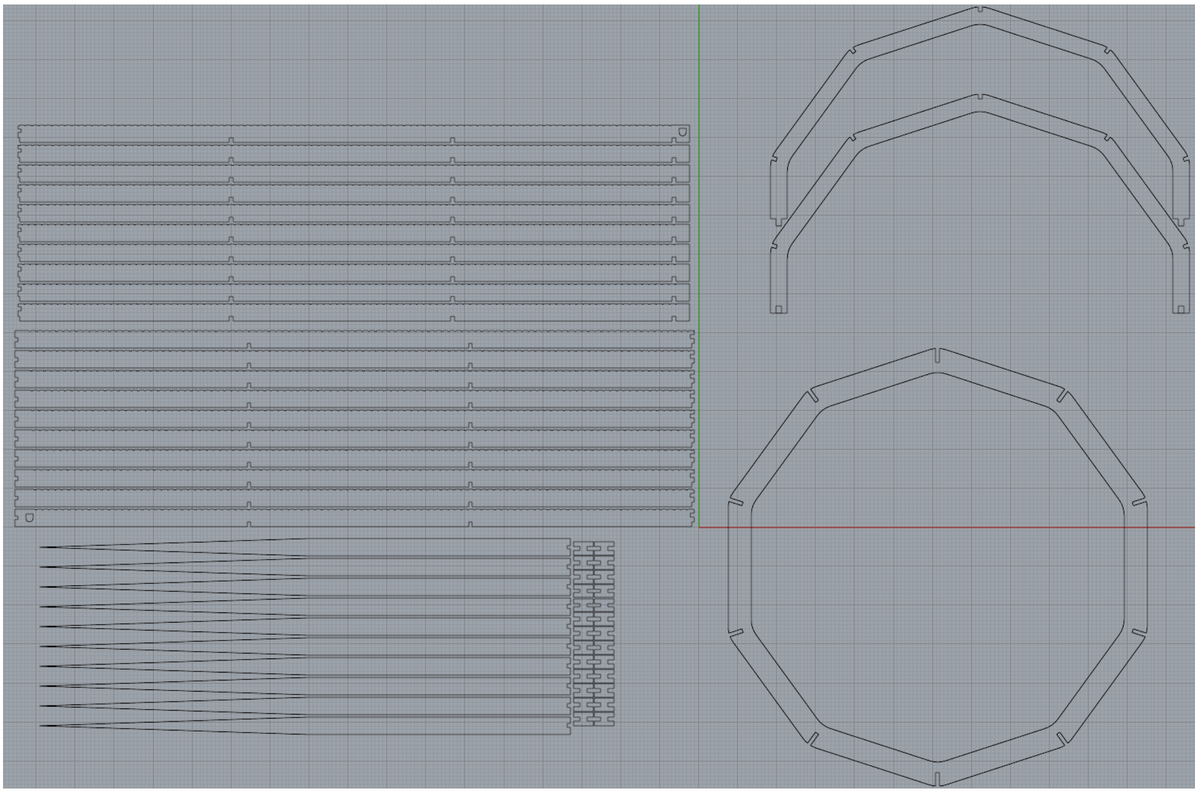

Figure A.2: Overview of the laser file used for the Cabauw campaign

B

Full code used for experimental data

Below, the full code for data processing is hosted. This code was used for the generation of all plots of the field data.

https://data.4tu.nl/private_datasets/6QKJMHl0UsXGtyGY_jrcWBHuwKQmDrS-zmhbX3rX4Wk